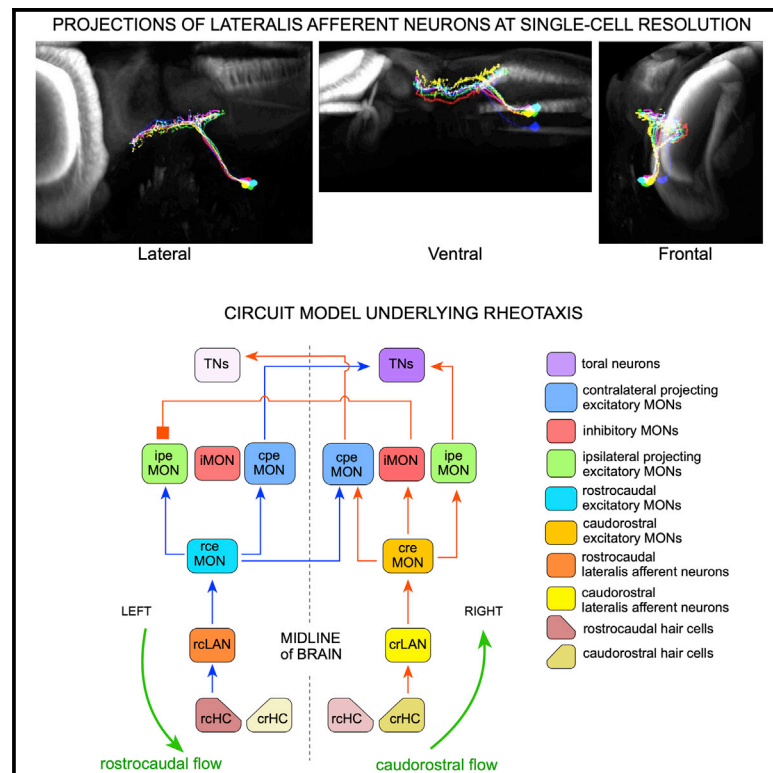


Current Biology

A neuronal blueprint for directional mechanosensation in larval zebrafish

Graphical Abstract



Authors

Gema Valera, Daniil A. Markov, Kayvan Bijari, ..., Giorgio A. Ascoli, Ruben Portugues, Hernán López-Schier

Correspondence

hernan.lopez-schier@helmholtz-muenchen.de

In Brief

Mechanosensation enables spatial orientation in the absence of visual references. Valera et al. produce a lateral-line projectome to generate a parsimonious circuit underlying rheotaxis in larval zebrafish. Integration of lateralized signals transmitted by direction-selective neurons underlies the encoding of water-flow direction in the brain.

Highlights

- Lateralis afferent neurons are structurally homogeneous in larval zebrafish
- Topographic representation of lateral-line receptors is not essential for rheotaxis
- Calcium imaging reveals unequal representation of water-flow direction in the brain



Article

A neuronal blueprint for directional mechanosensation in larval zebrafish

Gema Valera,^{1,6} Daniil A. Markov,^{2,6} Kayvan Bijari,⁴ Owen Randlett,⁵ Amir Asgharsharghi,¹ Jean-Pierre Baudoin,³ Giorgio A. Ascoli,⁴ Ruben Portugues,² and Hernán López-Schier^{1,3,7,*}

¹Sensory Biology and Organogenesis, Helmholtz Zentrum Munich, Germany

²Max-Planck Institute of Neurobiology, Munich, Germany

³Centre for Genomic Regulation, Barcelona, Spain

⁴Krasnow Institute for Advanced Study, George Mason University, VA, USA

⁵Department of Molecular and Cellular Biology, Harvard University, MA, USA

⁶These authors contributed equally

⁷Lead contact

*Correspondence: hernan.lopez-schier@helmholtz-muenchen.de

<https://doi.org/10.1016/j.cub.2021.01.045>

SUMMARY

Animals have a remarkable ability to use local cues to orient in space in the absence of a panoramic fixed reference frame. Here we use the mechanosensory lateral line in larval zebrafish to understand rheotaxis, an innate oriented swimming evoked by water currents. We generated a comprehensive light-microscopy cell-resolution projectome of lateralis afferent neurons (LANs) and used clustering techniques for morphological classification. We find surprising structural constancy among LANs. Laser-mediated microlesions indicate that precise topographic mapping of lateral-line receptors is not essential for rheotaxis. Recording neuronal-activity during controlled mechanical stimulation of neuromasts reveals unequal representation of water-flow direction in the hindbrain. We explored potential circuit architectures constrained by anatomical and functional data to suggest a parsimonious model under which the integration of lateralized signals transmitted by direction-selective LANs underlies the encoding of water-flow direction in the brain. These data provide a new framework to understand how animals use local mechanical cues to orient in space.

INTRODUCTION

Animals explore habitats to find food, mates or shelter. Spatial orientation during locomotion relies on sensory systems that acquire spatiotemporal changes in environmental cues¹. Vision is optimal for orientation because it provides a sense of motion relative to a fixed external reference frame. Yet, many animals can form an internal representation of movement using other sensory modalities. For example, the vertebrate vestibular system uses vectorial mechanosensation to inform the brain about linear and angular head motion². Also, fishes employ the mechanosensory lateral line to align swimming to water currents. This innate orienting behavior is called rheotaxis^{3–5}. Importantly, mechanosensation allows spatial orientation in the absence of visual cues, either in darkness or in the naturally blind^{6–9}. For instance, larval zebrafish use the superficial lateral line to exploit mechanical inhomogeneities in the local current to engage in counter-flow swimming without a visual reference frame⁵.

The lateral line is a distributed, lateral-symmetric sensory system formed by a collection of discrete organs called neuromasts¹⁰ (Figure 1A). Each neuromast contains two populations of mechanoreceptive hair cells, equal in number, which are plane-polarized along a single axis but in opposite directions (Figure S1A)^{11,12}. Because planar orientation determines the hair-cell's direction of maximal excitability, each neuromast is sensitive to opposing directions of water flow^{13–15}. Larval

zebrafish has around 50 neuromasts located in the head (anterior lateral-line / ALL), and along the trunk and tail (posterior lateral-line / PLL) (Figure 1A). The PLL consists of a majority of horizontal neuromasts whose axis of maximal sensitivity runs parallel to the animal's anteroposterior body axis^{12,16}. Larval ALL and PLL contain approximately 60 bipolar lateralis afferent neurons (LANs) each. LANs project peripheral fibers toward hair cells and central axons that split into an anterior and a posterior branch to arborize along the entire length of the ipsilateral hindbrain (Figures 1A and 1B and Figures S1B, S1D, and S1E). LANs central projections form a central lintel (LCL) with laminar organization, which coarsely represents the spatial distribution of neuromasts via a topographic (somatotopic) arrangement (Figures 1A and 1B)^{10,12,17}. Each neuromast is normally innervated by 4 LANs^{13,15,18}. As each LAN selectively synapses with multiple hair cells of identical orientation (Figures S1A and S1C), neurons are effectively tuned to a single direction of mechanical stimuli^{18–20}. LANs have a small receptive field restricted to the immediacy of the innervated neuromast, sampling ipsilateral local hydrodynamics²¹. Therefore, afferent pathway transmits in parallel the direction and localization of water motion²².

Rheotaxis has been studied for over 100 years^{23,24}. Yet, a neuronal wiring diagram of the lateral line does not exist. High-resolution mapping of projections and connectivity of neurons is an essential first step toward understanding the sensorimotor transformations that govern behavior^{25–31}. Here we use a



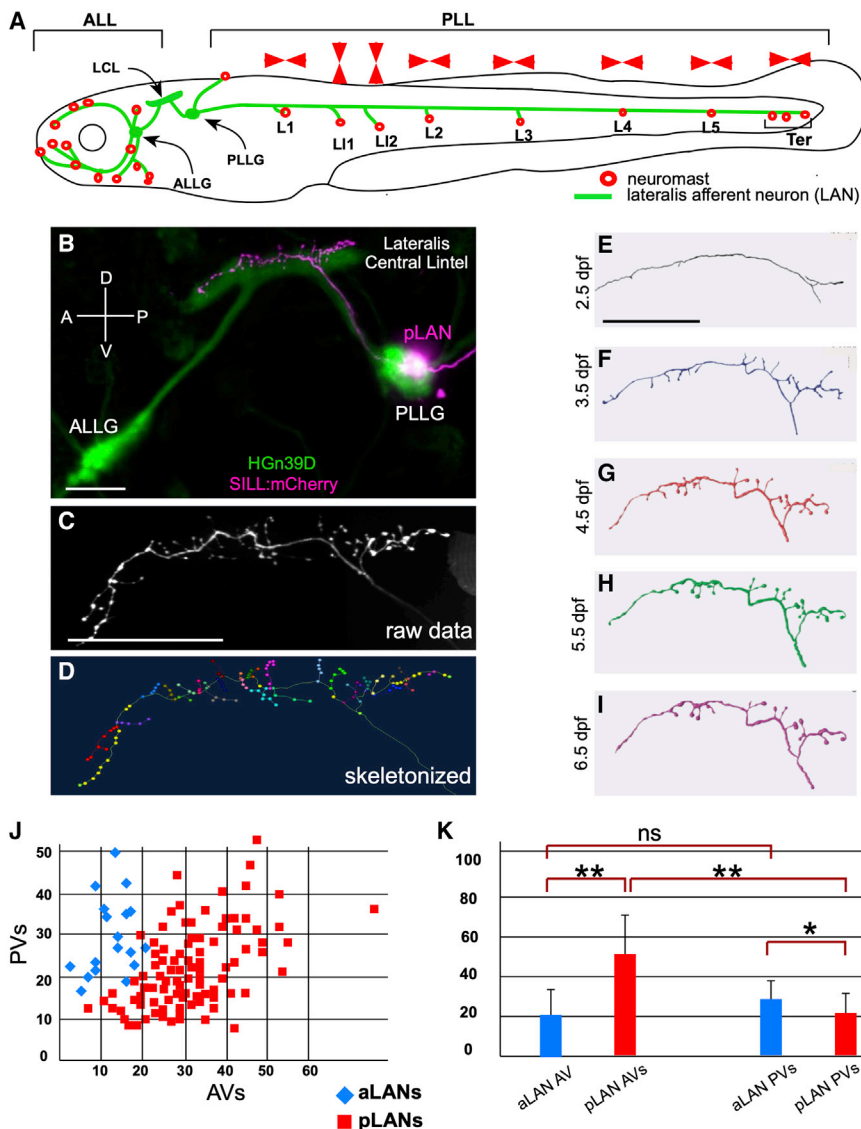


Figure 1. The lateral line in larval zebrafish

(A) Schematic representation of a larval zebrafish showing neuromasts (red circles) of the anterior (ALL) and posterior (PLL) lateral line. Posterior neuromasts are named (L for troncal and Ter for terminal), and the planar polarization of their constituent hair cells (horizontal or vertical) is indicated (red arrowheads). Lateralis afferent neurons (LANs) and the lateralis central lintel (LCL) are shown in green.

(B) Confocal image of a HGN39D transgenic larva (green) injected with Sill:mCherry (red), showing the neuronal soma of a posterior LAN (pLAN) within the posterior ganglion (PLLG) and its position within the LCL. The anterior ganglion (ALLG) is also shown.

(C) Structure of the central projection of an individually marked LAN.

(D) Skeletonization of the same projection shown in (C) with terminal varicosities marked with colored dots.

(E–I) Skeletonized central arbors of the same neuron over consecutive days from 2.5 to 6.5 days-post fertilization (dpf). In all panels, anterior is left and dorsal is up.

(J) aLANs and pLANs (respectively, blue diamonds and red squares) constitute distinguishable morphological classes according to the number of anterior and posterior varicosities (respectively AVs and PVs).

(K) Bar chart showing significant differences between aLANs (blue) and pLANs (red) for AVs and PVs. aLANs have similar number of AVs and PVs along the length of the central projection. Scale bars are 50 μ m. See also Figure S1.

directional tuning of each neuron (Figure S1C)¹⁸. The resulting raw images were stitched together and skeletonized (Figures 1C and 1D). Conveniently, the HGN39D transgene allows to precisely position LAN perikaria within lateral ganglia as well as the central arbors within a three-dimensional coordinate

system for registration onto a standard brain atlas³³ (Figures S1D–S1I and Video S1). We first defined when LANs become structurally stable by analyzing individualized specimens daily between 2.5 and 6.5 days-post-fertilization (dpf) ($n = 5$). We found that LAN central arbors stabilize at 5.5 dpf (Figures 1E–1I). Therefore, we chose to conduct a comprehensive projection mapping (projectome) in 6 dpf specimens. Conveniently, this stage enables cross-platform integration of our data because it coincides with the majority of neurobiological studies in zebrafish, including standard light- and electron-microscopic circuit reconstructions, brain atlases, whole-brain activity mapping, as well as most behavioral studies^{4,5,28,29,33–39}.

Architecture of anterior and posterior LANs

To generate a standard measure of neuronal structure and synaptic connectivity by fluorescent light microscopy we assessed the correlation between terminal-branch varicosities and synapses, respectively by co-expressing mCherry and Synapsin1-GFP

RESULTS

LAN growth and structural stability

We first established a pipeline to acquire three-dimensional structures of individual LANs in larval zebrafish at high resolution. To this end, we stochastically expressed a red-fluorescent protein in these neurons using the “Sill” enhancer in the double transgenic line Tg[Myo6b: β -actin-GFP ; HGN39D], which respectively highlight the hair-cells apical stereocilia and the entire LAN pathway with green fluorescence^{13,32}. Individually marked LANs were traced from the periphery to the brain by light microscopy^{13,19} (Figure 1B). Because LANs present a conspicuous arborization below neuromasts and stereotypic connectivity with hair cells, we could unambiguously assign both the spatial receptivity (localization of the innervated neuromast) and the

in individual LANs⁴⁰ ($n = 6$). We found that the number of varicosities and terminal branches relate linearly (Figure S1J). Most mCherry(+) varicosities and Synapsin1-GFP puncta co-localized (Figures S1K–S1N). Therefore, terminal varicosities can be used as a proxy for synapses for high-throughput acquisition of data in living specimens. Using singly labeled LANs, we obtained data for 176 individual neurons, from which we discarded 32 because we could not unambiguously define at least one the features used for classification (below), resulting in 144 high-quality structures. A first-pass analysis revealed that LANs of the anterior lateral line (aLANs) have simpler central arbors (mean varicosities \pm SD: 52.10 ± 14.56 , $n = 20$) than those of the posterior lateral line (pLANs) (mean \pm SD: 74.77 ± 24.27 , $n = 124$). aLANs have approximately half the number of anterior varicosities (AVs) than pLANs (respectively, 22.55 ± 9.89 and 52.27 ± 18.10) (Figures 1J and 1K). However, aLANs have only marginally more posterior varicosities (PVs) than pLANs (respectively, 29.55 ± 8.78 and 22.49 ± 9.12). Interestingly, we found two clear peaks of varicosities along central projections (Figures S1G and S1O), suggesting spatial-coincident output for the ALL and PLL.

Central-arbor structure and pLAN receptive field

We compared central arbors using three discrete features of LANs: hemispheric location (left or right side of the body), directional tuning (planar polarity of hair-cell partners) and spatial receptive field (localization of the innervated neuromast). Unsupervised cluster analysis showed that aLANs and pLANs represent discrete neuronal classes (Figure 2A). For further validation of the neuronal segregation, we systematically increased the number of target clusters (target neuronal classes) in the unsupervised algorithm from 2 to 11 and inspected the correspondence between the objective (blind) classifications obtained from unbiased morphometric quantification and the above features. When selecting two clusters, unsupervised clustering neatly separated aLANs from pLANs. This segregation persisted when increasing the number of clusters. For example, with three clusters (red, blue, and green colors in Figure 2A) the aLANs remained compactly in one group while pLANs split into two sub-groups. Yet, the sub-groups of pLANs (L1–L5 from trunk neuromasts and Ter from terminal neuromasts) did not systematically align with any combination of morphological measurements. aLANs and pLANs, by contrast, were only subdivided and never “reshuffled” upon increasing the number of target clusters, indicating that this unsupervised morphological partition was robust. To further check whether aLANs and pLANs formed discrete classes as opposed to constituting a continuum, we analyzed the distribution of the morphometric parameter with the highest load on the first principal component, namely Contraction, which quantifies arbor meandering or the tortuosity of the neurite path. The distribution of Contraction values over the entire population of neurons was clearly bimodal (Figure 2B), confirmed quantitatively by Komogorov-Smirnov tests ($p < 0.05$). Moreover, the distributions of Contraction values corresponded with the two peaks of the bimodal distribution, confirming the discrete nature of aLANs and pLANs.

Next, we analyzed the data by ensemble supervised learning applied to binary classification. In line with the results of unsupervised clustering, aLAN and pLAN axons could be separated with 99% accuracy. The morphometric features that contributed

most to this discrimination were size-related, with aLAN arbors generally being longer and farther reaching than the pLAN arbors. Thus, aLANs and pLANs can be identified on the stereotypy of their central arbors (Figure 2C). pLANs innervating neuromasts in the trunk (L1–L5) could be separated from neurons innervating the terminal (Ter) neuromasts in the tail with intermediate accuracy (75%), mainly on the basis of branch complexity (number of bifurcations) and span (height and width) (trunk versus tail) (Figure 2C). pLAN directional tuning (rostr-caudal- and caudo-rostral-tuned, respectively rcpLANs and crpLANs) could be separated only marginally (64% accuracy), mainly based on local features (bifurcation angles, fractal dimension, and tortuosity) (rostral versus caudal) (Figure 2C). Interestingly, when considering only the L1–L5 pLANs, the accuracy of separation by directional tuning increased to 91% (rostral versus caudal, trunk only) (Figure 2C). Ter pLANs, by contrast, achieved a more modest gain in accuracy (65%), on the basis of bifurcation angle (rostral versus caudal, tail only) (Figure 2C). Thus, we tested if the distinction between L1–L5 and Ter could be improved by disjointly considering LANs based on directional tuning. rcpLANs could be separated in L1–L5 and Ter with a slightly improved accuracy (80%) based on arbor width (not illustrated). For crpLANs, separation remained unaltered (78%), but the underlying features changed (partition asymmetry, branch order, and bifurcation angles). Lastly, axonal projections from the right and left hemispheres showed the poorest separation (61% accuracy) based on number of bifurcations and span (width and Euclidian distance) (right versus left) (Figure 2C).

In the persistent diagram vector analysis, we first computed the pairwise distances between all 144 neurons based on the dot-product arccosine (Figure 2D). Then we tested whether the within-group distances were statistically different from those across-groups for the several groupings (aLAN/pLAN, rc/cr pLAN, right/left pLAN, and L1–L5/Ter). The results unequivocally corroborated that only the aLAN and pLAN groups displayed significantly less-distant vectors when comparing “like neurons” (aLAN with aLAN and pLAN with pLAN) than when comparing mixed pairs (aLANs with pLANs) (Figure 2D). We next addressed pLANs’ spatial receptive field by dividing 115 high-quality neuronal structures into 6 groups according to the identity of the innervated neuromast: L1 ($n = 13$), L2 ($n = 16$), L3 ($n = 18$), L4 ($n = 20$), L5 ($n = 11$) and Ter ($n = 37$). We found that the number of terminal varicosities was invariant across all groups (L1 = 74.23 ± 23.11 ; L2 = 81.31 ± 29.59 ; L3 = 74.33 ± 17.07 ; L4 = 76.30 ± 20.80 ; L5 = 78.27 ± 28.05 and Ter = 71.89 ± 26.31). We did not find inter-group differences for anterior varicosities ($2.29F_{crit} > 0.52F$; p value = 0.761099 [ns]; $\alpha = 0.01$) and posterior varicosities ($2.29F_{crit} > 0.38F$; p value = 0.861375 [ns]; $\alpha = 0.01$). This result is surprising because each Ter pLAN innervates a cumulative total of approximately 30 hair cells in multiple neuromasts, whereas each L1–L5 pLAN innervates approximately 10 hair cells in individual neuromasts. Together, these data indicate that central-arbor structure discriminates aLANs from pLANs but cannot predict pLANs receptive field.

Central-arbor structure and pLAN directional tuning

We analyzed varicosities of caudo-rostral [cr]- and rostro-caudal [rc]-tuned pLANs, respectively crpLANs and rcpLANs innervating each of the troncal neuromasts (L1 to L5): L1cr ($n = 9$)

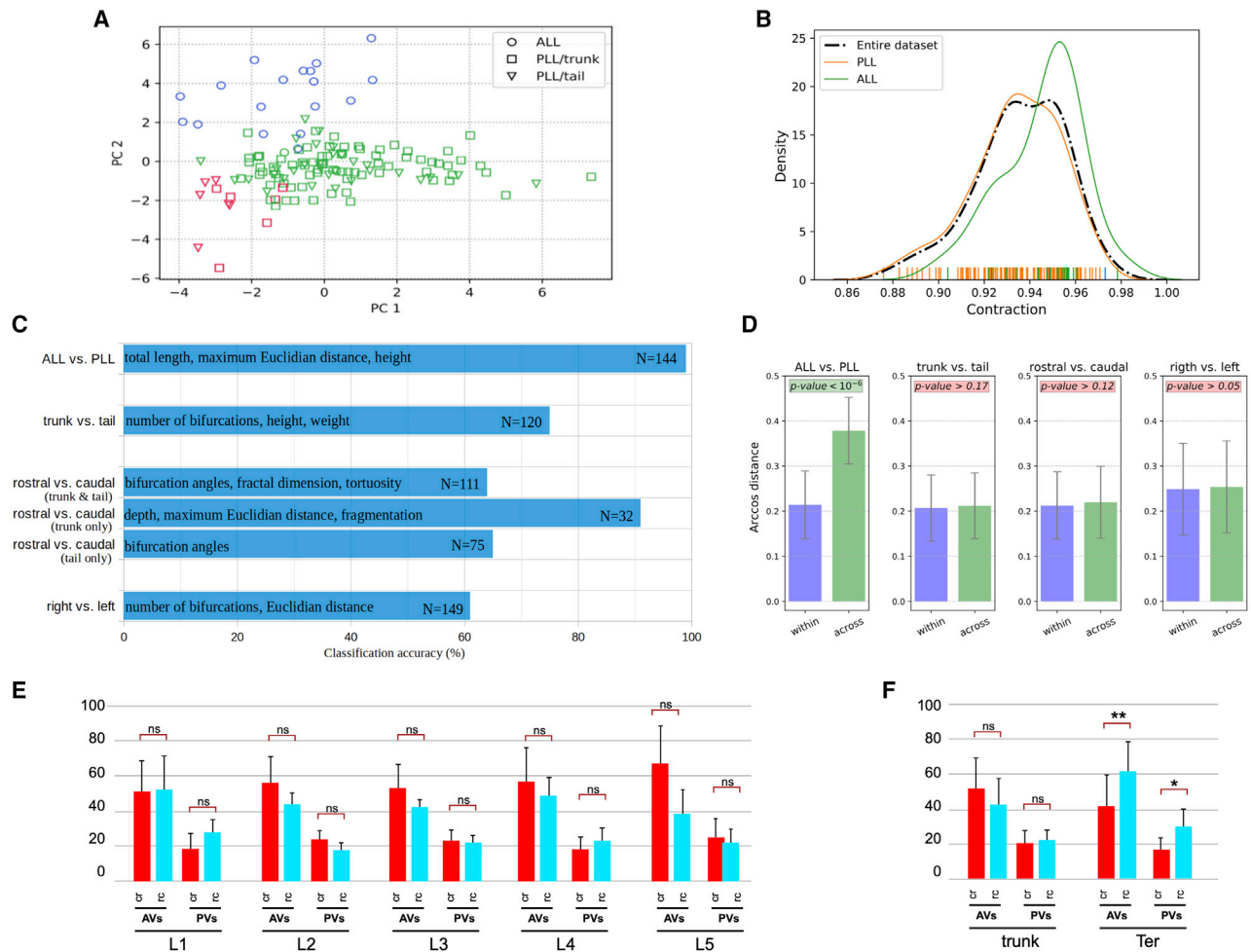


Figure 2. Morphometric analysis and classification of LANS

(A) Distribution of original neuron type labels projected onto the first two principal components (PC) according to unsupervised Gaussian Mixture Models clustering based on morphometrics. The only clear alignment is with a 2-class separation, which matches ALL (aLANs) and PLL (pLANs).

(B) Probability distribution functions of Contraction values (which measure neuronal branch tortuosity or meandering) for the whole cell population and for ALL and PLL neurons separately. The ALL and PLL distributions correspond to the peak of the bimodal Contraction distribution, confirming discrete rather than continuum classes.

(C) Classification accuracy (expressed as percent correct on the horizontal scale) for distinguishing between various subsets of axonal projections based on their morphometric parameters. The most discriminant features are reported in each case along with the sample size corresponding to each grouping.

(D) Persistence diagram vector analysis demonstrates that only aLANs/pLANs arcossine distances were statistically smaller within classes than across classes.

(E) Comparison of the number of AVs and PVs between caudorostral pLANs (crpLANs, red) and rostrocaudal LANS (rcpLANs, blue).

(F) Comparison of AVs and PVs between crpLANs (red) and rcpLANs (blue) in LANS from L1 to L5 analyzed as a whole (L1-L5_pLANs) and terminal LANS (Ter-LANS).

See also Figure S2 and Video S1.

versus L1rc (n = 4); L2cr (n = 9) versus L2rc (n = 4); L3cr (n = 11) versus L3rc (n = 6); L4cr (n = 11) versus L4rc (n = 7) and L5cr (n = 5) versus L5rc (n = 5) (Figure 2E and Figure S2). Despite a general bias of crpLANs toward more synaptic contacts, the difference within neuromasts or between neuromasts were statistically not significant (Figure 2E and Figure S2). Consolidating L1-L5 (trunk pLANs) increased the bias for individual pLANs, but only marginally. Finally, we analyzed Ter and found that Ter_crpLANs (n = 16) had fewer anterior and posterior varicosities than Ter_rcpLANs (n = 16) (Figure 2F). Thus, central-arbor structure is not a reliable predictor of pLANs directional tuning.

Lateral-line somatotopy is dispensable for rheotaxis in laminar water flow

Topographic maps are common in sensory systems, including the lateral line^{10,12,17,19,41–43}. To analyze in detail lateral line topography (somatotopy) we co-registered individual pLANs of the trunk (L1-L5 group) and tail (Ter group) using HgN39D as a landmark for a local coordinate system, which was subsequently registered to a reference brain³⁵. We found crisscrossing of terminal branches in the dorsoventral and the mediolateral axes of the hindbrain (Figures 3A and 3B). The same result was obtained L2 and the Ter pLANs were labeled with magenta- and

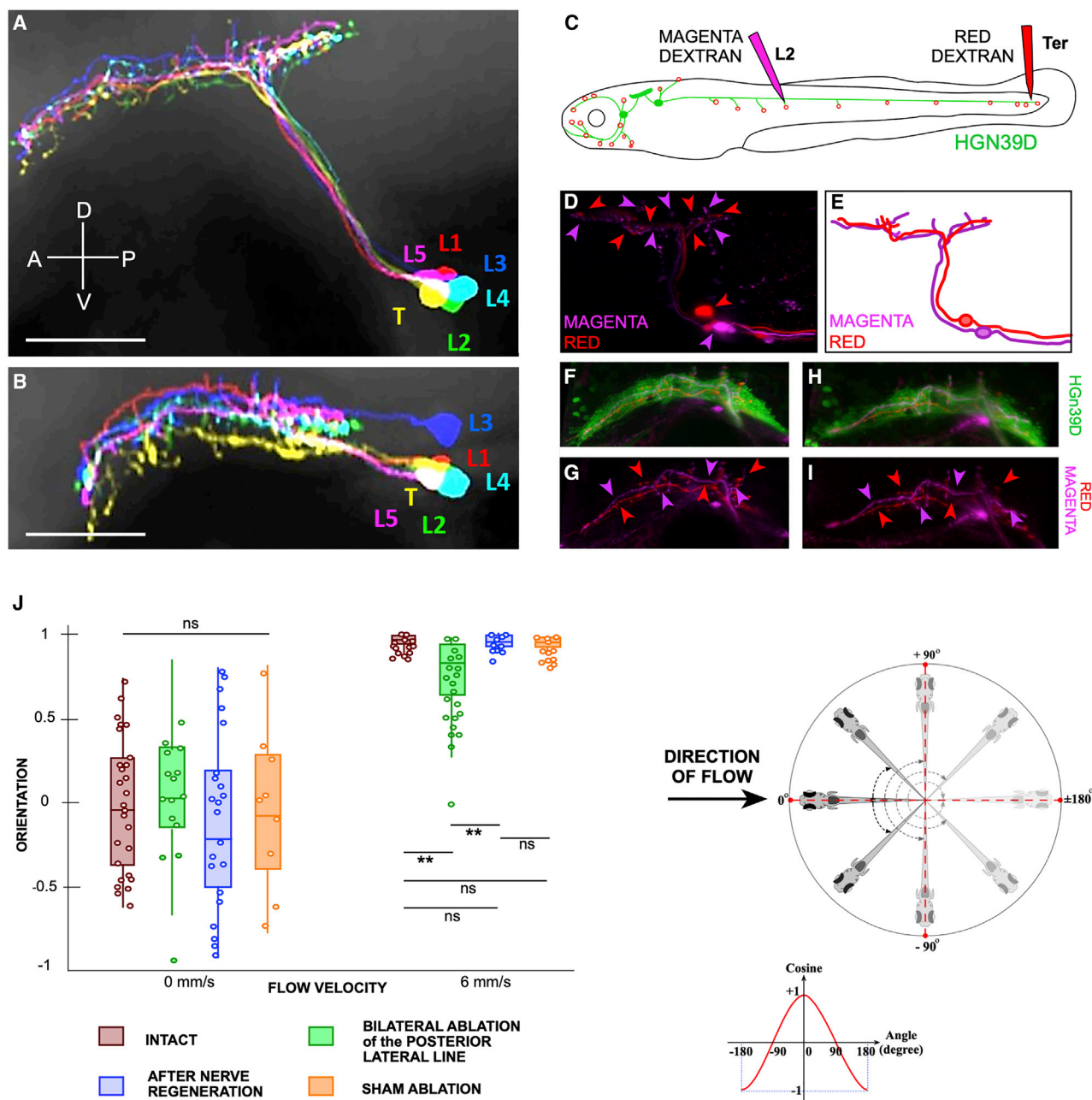


Figure 3. Lateral-line topographic map and rheotaxis

(A and B) Volume-filled skeletons of 6 pLANs morphed onto a reference brain. Each pLAN innervates a different neuromast: L1 (red), L2 (green), L3 (blue), L4 (cyan), L5 (magenta) and Ter (yellow). (A) Side view and (B) top view. The central projections crossed one another along the length of the hindbrain.

(C) Scheme of a double injection of a larval zebrafish with magenta and red dextrans, in HGN39D (green). Magenta dextran is injected into the L2 neuromast to label only L2_pLANs. The red dextran is injected into the terminal neuromasts to label only Ter_pLANs.

(D) Maximal projection of the central projections of pLANs labeled with magenta and red dextrans, showing with corresponding-color arrowheads the central projections of L2_pLANs and Ter_pLANs relative to one another. The somata of the labeled neurons are indicated with color-coded arrowheads. Note that somatotopy is not precise along the LCL.

(E) Scheme of the projections shown and color-coded in (D).

(F and G) Central projections of a red- and a magenta-labeled axon within the background of the HGN39D transgenic line that labels the LCL with EGFP (green) (F). Color-coded arrowheads indicate the relative position of each axonal projection along the LCL (G).

(H and I) Same specimen after the severing and regeneration of the peripheral axons, revealing that central axons do not change relative position along the somatotopic axis despite peripheral rewiring (I).

(J) Orientation of intact and manipulated specimens at 6dpf under no flow (left hand-side, or under laminar water flow at 6mm/s (right hand-side). Scale bars are 50 μ m.

See also [Figure S3](#) and [Videos S2](#) and [S3](#).

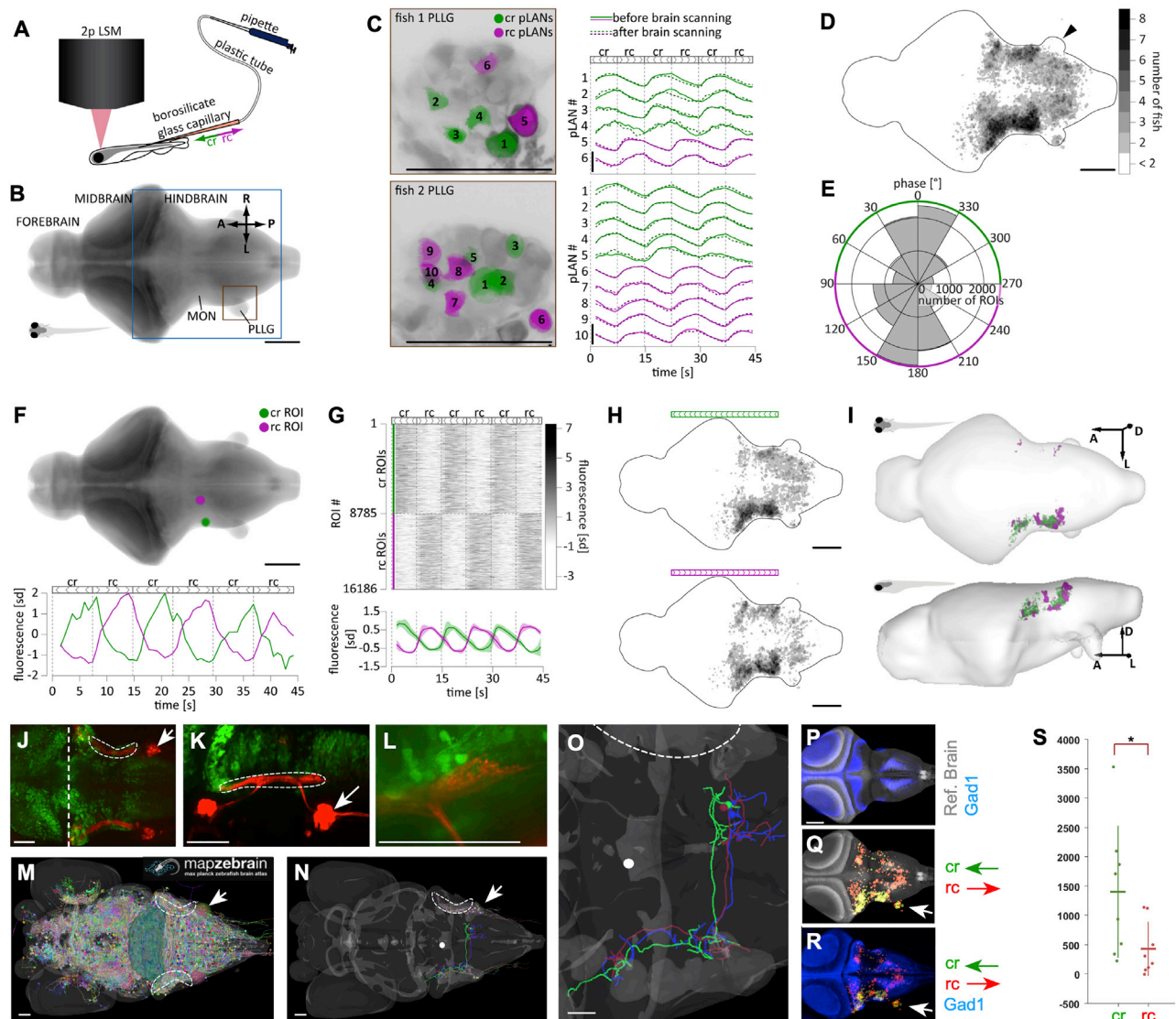


Figure 4. Brain responses to unilateral directional stimulation of neuromasts

(A) Stimulation and acquisition setup including two-photon laser scanning microscope (2p LSM), and the stimulation capillary.

(B) Maximal z-projection of the reference brain with the region that was imaged boxed in blue. Orange box shows the location of the PLLG ipsilateral to the stimulation side. MON – Medial Octavolateralis Nucleus. A – anterior, L – left, R – right, P – posterior.

(C) Activity of individual pLANs in the PLLG ipsilateral to the stimulation side in two larvae before and after whole-brain scanning. Green and magenta colors show location of responsive cr and rc pLANs, respectively. Traces show z-scored fluorescence of respective pLANs averaged across planes. Note that after whole-brain scanning, the responses of pLANs to stimulation remained similar to the initial responses.

(D) Location of all responsive ROIs. Black arrowhead indicates that there were no responsive ROIs in the contralateral PLLG.

(E) Bimodal distribution of the phase of the power spectrum frequency component corresponding to the stimulation frequency (see Methods for details).

(F) Two example cr- and rc-selective ROIs.

(G) Activity of all cr- and rc-selective ROIs detected in all imaged larvae. The bottom image shows activity, averaged across animals; shaded areas denote SEM across larvae.

(H) Location of all cr- and rc-selective ROIs in the reference brain. Color map is the same as in D.

(I) Anatomical regions of the reference brain that contained cr- and rc-selective ROIs consistently across larvae.

(J and K) A maximal projection confocal image of a Gad1b-EGFP (green) ; Sill:Cherry (red) double transgenic fish at 6dpf (dorsal view in J and lateral view in K) showing the relative position of the LAN central lintel (dashed areas). Midbrain-hindbrain boundary is shown by a vertical dashed white line, and PLL ganglion by a white arrow.

(L) A magnification of a portion of the LAN central projections (red) and Gad1b(+) neurons (green), showing spatial proximity.

(M) Snapshot of a dorsal view of a larval zebrafish reference brain, taken from the mapZebbrain Atlas database, depicting all available single-neuron traces. Dashed area indicates the position of the LAN central lintel and white arrow the position of the PLLG.

(N) Same reference brain with 3 Gad1(+) neurons overlaid, colored green (ref. 12387), blue (ref. 12352) and red (ref. 12344) in the mapZebbrain Atlas. The white dot is an arbitrary spatial reference used to evaluate neuronal projection is three-dimensional renderings (not shown).

(legend continued on next page)

red-fluorescent dextrans and registered against one another (Figures 3C–3E). Therefore, point-to-point spatial representation of the posterior neuromast array is imprecise. To test lateral-line somatotopy functionally, we used a combination of pLAN map rewiring and a rheotaxis assay. In previous studies, we found that after peripheral nerve transection LANS regenerate axons to re-innervate neuromasts within 36 h^{18,44}. Regenerating axons reproduce synapses with hair cells of the original planar polarization, recapitulating neuronal directional tuning^{18,44}. However, they nearly always re-innervate a neuromast different from the original with a strong bias toward more caudal neuromasts, which strongly disrupts lateralis somatotopy¹⁸. Using this assay, we first tested whether central plasticity may compensate the resulting abnormal topography. We labeled the L2 pLANs and the Ter pLANs, respectively with magenta- and red-fluorescent dextrans, cut their peripheral axons, and examined specimens 3 days later (Figures 3F–3I). We found that despite extensive topographic changes in the periphery, the organization of the central arbors remained unchanged. Next, we asked if the resulting disrupted somatotopy produces rheotactic deficits by performing a controlled behavioral test using laminar water flow in the absence of visible light⁵ (Figures S3A–S3E). Under such condition, rheotaxis can be quantified by measuring the orientation of larval zebrafish relative to the direction of water flow using high-speed video recordings (Figures S3F and S3G). Under no flow, animals do not show any particular orientation (Figure 3J and Figure S3F; Video S2). As shown previously⁵, a laminar water current of 6mm/s elicits a robust counter-flow orientation (Figure 3J and Figure S3G; Video S3). Simultaneously severing all PLL axons on both sides of the fish (bilateral posterior ablation = BPA) ($n = 8$ larvae / 75 trials) significantly reduced rheotaxis (Figure 3J). Upon axon regeneration (REGEN) ($n = 10$ larvae / 103 trials), rheotactic performance recovered to levels indistinguishable from those of untouched (INTACT) ($n = 6$ larvae / 60 trials) and sham-ablated (SHAM) larvae ($n = 6$ larvae / 70 trials) (Figure 3J). For no-flow conditions, we used INTACT ($n = 2$ larvae / 30 trials), BPA ($n = 5$ larvae / 20 trials), REGEN ($n = 10$ larvae / 30 trials), and SHAM ($n = 5$ larvae / 13 trials). Confidence levels for pairwise comparisons are $^{**}p < 0.01$, $ns\ p > 0.05$. We conclude that somatotopy is not generally essential for rheotaxis by larval zebrafish.

Brain responses to directional mechanical stimulation of neuromasts

Because structural differences in the afferent pathway cannot explain how the lateral line resolves the directional ambiguity of the periphery, we decided to examine neural activity in the brain upon directional mechanical stimulation of neuromasts. We developed a preparation that allows brain-wide calcium imaging by scanning two-photon microscopy during stimulation

of a single or two adjacent troncal neuromasts, sequentially in the caudorostral and rostrocaudal direction (Figure 4A and Figures S3H–S3K). After segmenting imaging data into ROIs (see Methods)^{45,46}, we ascertained that directional stimulation of a neuromast elicited specific and consistent activation of pLANs by measuring calcium transient of ROIs detected in the posterior lateralis ganglion (PLLG) (Figure 4B). We observed that 2 to 5 pLANs responded in a direction-selective manner to directional stimuli (Figure 4C). These responses remained stable throughout the whole 1 h period of brain scanning, demonstrating the stability of the preparation. Focusing on the first output region of the lateral line within the hindbrain, the Medial Octavolateralis Nucleus (MON) and the medulla oblongata^{47–51}, we identified all ROIs with consistent responses (regardless of stimuli direction). Responsive ROIs were located predominantly within the target area ipsilateral to the stimulation side. However, the contralateral MON also contained a significant fraction of responsive ROIs (Figure 4D). The contralateral PLLG did not respond to stimulation (black arrowhead in Figure 4D), suggesting contralateral projections within the hindbrain. To assess directional preference of responsive ROIs, we performed fast Fourier transformation on the fluorescent traces and found that the phase of the frequency component corresponding to the stimulation frequency follows a bimodal distribution. This allowed us to divide all responsive ROIs into cr- and rc-selective clusters (Figure 4E). Two example cr and rc ROIs are shown in Figure 4F. The clusters were roughly equal in size (in total, 9795 cr ROIs and 7401 rc ROIs in all imaged larvae, Figure 4G). Both types of ROIs were located predominantly on the ipsilateral side of the hindbrain (Figure 4H). We then identified brain regions with consistent-across-fish directional preference (Figure 4I). We found that for both directions of stimulations, consistent regions were located predominantly on the ipsilateral side of the brain (44'225 μm^3 cr ipsilateral, 300 μm^3 cr contralateral, 25'465 μm^3 rc ipsilateral, 1'506 μm^3 rc contralateral). Thus, a given cr-selective unit is located on the ipsilateral side of the brain with a mean probability of 99.33%. The average number of cr-selective units on the ipsilateral side is therefore 44'225 and the expected variance in this measurement is 298 (standard deviation = 17). If bilateral distribution of cr- and rc-selective units is the same, the expected number of rc-selective units on the ipsilateral side of the brain is 26'790, which is ~ 76 standard deviations away from the observed number. We conclude that even though stimulation at either direction activated more consistent voxels on the ipsilateral side of the brain than on the contralateral, the bilateral distribution of cr- and rc-selective units is asymmetric across the midline, with a much larger fraction of rc-selective units being found on the contralateral side to the stimulation, compared to the cr-selective units.

(O) Magnification of the neurons shown in (N). All 3 Gad1(+) neurons project contralaterally within the hindbrain.

(P) Reference brain (gray) overlaid with Gad1(+) neurons.

(Q) Reference brain (gray) overlaid with functional cr or rc maps (respectively, green and red). White arrowhead indicates the posterior lateralis ganglion ipsilateral to the mechanical-stimulated side of the fish. Note lack of calcium signal on the contralateral ganglion.

(R) Gad1b stack overlaid with functional cr or rc maps (respectively, in green and red, whose overlap is yellow).

(S) The number of active voxels overlapping with the Gad1b binary mask. Each fish contributes one point to each category in the x axis, the horizontal line denotes the mean number of voxels across fish and the vertical line denotes the standard deviation. p value = 0.0281 (Mann-Whitney-U-Test).

Scale bars are 100 μm in (A)–(I) and 50 μm in (J)–(R). See also Figure S4.

Hindbrain areas responsive to directional stimulation of neuromasts

Increased activation of the contralateral hindbrain in response to rc stimulation compared to cr stimulation may result from cross-midline inhibition, consistent with previous studies in several teleosts showing inhibitory neurons in deep layers of the medulla and MON^{51–54}, the expression of inhibitory-neuron metabotropic glutamate receptor GluRd2/Grid2 in the MON^{52,55}, and pLAN input to neurons expressing the inhibitory neuronal marker Glutamate Decarboxylase-1/2 (Gad1/2)⁵². To test this possibility in larval zebrafish, we generated a double transgenic line that expresses EGFP under the Gad1b promoter⁵⁵ and RFP in LANs¹⁹. Analyzed at 6 dpf, these specimens showed juxtaposition of LANs central lintel (LCL) and Gad1b:EGFP at the level of the MON (Figures 4J–4L), but does not confirm direct connectivity between LANs and Gad1b(+) neurons. It has been shown that Gad1/2(+) neurons in adult zebrafish project to the contralateral hindbrain⁵². Using publicly available comprehensive datasets of single neurons in larval zebrafish²⁸, we found contralateral projections of individual Gad1b(+) in the zebrafish larva (Figures 4M–4O), supporting cross-midline inhibition.

Next, we registered calcium-imaging data onto the brain of a Gad1b:EGFP transgenic specimen (Figures 4P–4R) by creating a binary mask of Gad1b signal from the Z-Brain Atlas³³, and computed the number of caudorostral- and rostrocaudal-active voxels overlapping with the mask (Figures S4A and S4B). We found that hindbrain areas responding to unidirectional stimulation in either direction overlap with the Gad1b signal (Figures 4P–4R). Yet, the number of caudorostral-active voxels overlapping with the Gad1b mask was significantly higher than of rostrocaudal-active voxels (Figure 4S, *p* value: 0.0281), suggesting that caudorostral stimulation activates inhibitory neurons in the hindbrain to a much greater extent than rostrocaudal stimulation. To further test this conclusion, we stimulated the posterior lateral line in the caudorostral and rostrocaudal direction using a set-up similar to that employed for rheotaxis, but in which animals are held in place with a glass capillary. After stimulation, animals were quickly fixed and stained with a combination of antibodies that reveal the phosphorylation status of ERK, a kinase which has previously been used to identify active neurons in zebrafish brain³³. Phosphorylated-ERK (pERK) of non-stimulated fish showed low-level homogeneous background signal (Figures S4C and S4D). By contrast, stimulated specimens revealed strong punctate staining in a fraction of Gad1b(+) neurons. Consistent with calcium-imaging data, pERK signal from rostrocaudal stimulations did not show any obvious lateral asymmetry in the hindbrain.

DISCUSSION

Zebrafish as young as 5 days of age use lateral-line mediated mechanosensation to perform rheotaxis under laminar water currents in the absence of visual cues⁵. This is surprising because when immersed in a flow that is uniform in space and time, it is not possible for the fish to detect currents in the absence of an external fixed reference frame. An elegant solution to this problem posits that larval zebrafish uses the posterior lateral line (PLL) to sense changes in the vorticity of the local flow to determine the direction of the water current⁵. The

proposed behavioral algorithm, however, rests on three assumptions⁵. First, that topographic mapping of the lateral line onto the brain is dispensable because the neuromasts of the PLL act as a consolidated unit. Second, the existence of direction-selective central units. Third, inter-hemispheric integration of direction-specific signals. To test these postulates, we constructed a comprehensive cellular-resolution lateralis afferent neuron (LAN) projectome, assayed the behavioral impact of acutely disrupting posterior LANs (pLAN) topography, and imaged neuronal activity in the hindbrain during directional stimulation of neuromasts. We found a remarkable structural homogeneity among pLANs, that somatotopy is dispensable for rheotaxis under laminar currents, and evidence of lateralized brain responses to directional water flow. These data allowed us to develop a parsimonious model circuit underlying rheotaxis. We discuss below the supporting evidence.

The lateral-line projectome

Early evidence supports the idea that somatotopy may be used to represent a directional current in the form of an accurate spatial transformation of the temporal sequence of stimulation of neuromasts along the animal's body. For instance, neurons located in the lateral part of the Medial Octavolateralis Nucleus (MON) of goldfish respond maximally to stimulation of neuromasts on the rostral part of the fish, whereas neurons located in the medial part of the MON to more caudal neuromasts^{56,57}. Yet, our results indicate that lateralis somatotopy is not essential for rheotaxis. Another possibility to represent flow direction is via asymmetric transmission of rostrocaudal and caudorostral flow, possibly through stereotypic differences in projections between LANs. However, we found remarkably low structural variability among LANs. This is consistent with the similarities among LANs seen in electron-microscopic neuronal reconstructions in one zebrafish larva³⁶. Altogether, these findings do not support the hypothesis that stereotypic structural differences within the pLAN pathway play a major role in rheotaxis by larval zebrafish under laminar water currents⁵.

Activity of lateral-line responsive neurons in the hindbrain

An alternative solution to disambiguate flow direction is via the combined responses of an ensemble of excitatory and inhibitory neurons receiving parallel channels of directional mechanical information, together with a memory unit that compares current and previous input, as suggested by the behavioral algorithm⁵. Because the posterior lateral line detects the direction of water flow independently on each side of the animal, hemispheric signals must be transmitted to the contralateral side of the brain for bilateral integration⁵⁸. This idea requires the existence of direction-tuned central units as well as inter-hemispheric crossover. In several teleosts, ascending fibers originating in lateral-line responsive crest neurons of the MON and in the medulla project to the contralateral nucleus medialis of the Torus Semicircularis (TS)^{50,52}, to eventually reach the diencephalic Optic Tectum^{59,60}. Notably, only a small fraction of lateral-line responsive neurons in the TS are sensitive to water-flow direction in goldfish, suggesting that integration of directional signals occurs in the hindbrain^{56,57}. Similar observations have been made in larval zebrafish using whole-brain calcium imaging⁶¹, suggesting the existence of

monodirectional-tuned and direction nonselective neurons within and around the MON, as well as direction nonselective neurons in the torus and tectum, indicating that a large proportion of directional signals are integrated in the hindbrain. Some LAN-responsive MON neurons in goldfish and zebrafish are Gad1(+) inhibitory GABAergic⁵². The lateralized representation of flow direction that we found encompass areas that include a population of lateral-line responsive Gad1(+) neurons. We also find evidence of contralateral projecting Gad1(+) neurons in the hindbrain. These neurons are located immediately adjacent to the MON in the dorsal medulla, which has been reported to contain central inhibitory neurons of lateral-line input in goldfish⁵⁴. Early local inhibition may suppress transient fluctuations due to local turbulence, or enhance contrast between different directions of water flow¹⁴. However, our data suggest an additional possibility, that contralateral inhibition suppress the response of a subpopulation of excitatory neurons carrying same-direction information, to enable integration of opposing directions of the lateral-line stimulation from the left and right sides of the fish.

A realistic circuit model for rheotaxis by larval zebrafish

We formulate the first circuit model for lateral-line mediated rheotaxis (Figure 5). We arrived to this model by iterating the simplest possible architectures constrained by the data that we presented above, and incorporating all previous anatomical, physiological and behavioral findings in several teleosts^{7–9,12–14,16,31,39,44,45,47,51–55,57–59}. Crucially, the model provides the bases for the representation of radial velocity gradients (vorticity) in the zebrafish brain (Figure 5A), on which the behavioral algorithm that larval zebrafish uses to perform rheotaxis is grounded⁵. Our model proposes that neuronal activity elicited by direction-tuned hair cells (HCs) and pLANs is organized as segregated receptive fields (Figure 5B). The proposed circuit has been arbitrarily designed for counter-clockwise (ccw) flow to drive the TNs on the right hemisphere, and clockwise (cw) flow to drive the TNs on the left. The input structure predicts the existence of several hindbrain neuronal classes. First, direction-tuned excitatory MON neurons (eMONs), respectively rostrocaudal- (rceMONs) and caudorostral-tuned (creMONs)⁵³. The eMONs are relay elements that are necessary because LANs project exclusively ipsilaterally, whereas lateral-line responding neurons in the hindbrain are located both ipsi- and contralaterally to the stimulated neuromasts. rceMONs transmit directional information to both ipsilateral and contralateral projection excitatory MON/medullary neurons (respectively ipeMONs and cpeMONs) (Figure 5B), which may be the Zic1(+) neurons found in zebrafish and goldfish⁵². By contrast, creMONs relay information mainly ipsilaterally to ipeMONs and to inhibitory neurons (iMONs), which we suggest are GABAergic Gad1b(+). iMONs project contralaterally and inhibit ipeMONs to prevent symmetric bilateral activation of lateral-line responsive neurons in higher brain areas, likely in the TS, upon rotational flow⁵. Hence, TNs activation would only occur after receiving coincident excitatory input from opposite-tuned ipeMONs and cpeMONs. This is consistent with paucity of direction-tuned neurons in the torus^{57,61}. Thus, TNs will show direction-nonselective responses from integrated lateralized directional information.

Under laminar water flow zebrafish swims in bouts across the horizontal plane, experiencing an increase (blue-to-red transition

in Figure 5C) or decrease (red-to-blue transition) in the magnitude of local rotational flow (depicted as a rainbow horizontal bar), which is directly linked to the gradient of bulk water flow. Importantly, animals use this swimming strategy to compare rotational flow regimes in consecutive interbouts⁵. Larval zebrafish will continue swimming straight every time it experiences a decrease in gradient, but will perform a high magnitude turn in the direction of flow-field rotation magnitude if it faces an increase in gradient magnitude. Our circuit captures this behavior because if the magnitude of local rotational flow decreases (red-green-blue transition of the circular arrows in Figure 5C) the hemispheric difference of lateral-line mediated information that reaches the brain decreases (different shades of lilac in the brain), whereas if the magnitude of local rotational flow increases (blue-to-green-to-red transition) the hemispheric difference of lateral-line mediated information increases, generating a direct readout of changes in gradient that the fish uses to determine flow direction. The model circuit also explains the behavior of the fish when it experiences reversal of rotation flow upon its own directional changes across the horizontal plane. For instance when crossing the midline of the flowing column of water (as exemplified in Figure 5D), or when performing high-amplitude rotational swim bouts. In both cases, the system would simply undergo a mirror symmetric reversal of information reaching the brain. In addition, our circuit explains why the neuronal computations underlying rheotaxis do not operate under symmetric bilateral flow⁵. It is because if flow is lateral symmetric (Figure S5), both sides of the lateral line transmit identical information, which will effectively inform the brain that water is flowing but will not suffice for the animal to determine flow direction because the system remains directionally ambiguous in that cw and ccw flow generates identical inter-hemispheric information. Here, iMONs-mediated inhibition to ipeMONs to prevent the firing of TNs in the presence of lateral-symmetric water flow in the caudorostral direction, and to maintain symmetric TNs firing in the presence of lateral-symmetric rostrocaudal flow. Interestingly, whole-brain calcium imaging further supports this conclusion because hemispheric asymmetry in brain activity was not noted in larval zebrafish exposed to lateral symmetric flow (of note, asymmetry of node distribution from graph analysis of calcium imaging was associated to biased signal acquisition from light-sheet imaging)⁶¹. Finally, our circuit incorporates coincident excitatory input from both hemispheres, for the brain to display directional non-ambiguous activity only upon bilateral opposite flow direction, regardless of curl sign (cw or ccw) (Figure S5). Therefore, it also provides a simple explanation for why the animal needs simultaneous opposite-direction signals from both sides of its body, as evidenced by the observation that unilateral elimination of the posterior lateral line severely impairs rheotaxis⁵.

We emphasize that the proposed circuit assumes that neuromasts are equally sensitive to water flow in the headward (caudorostral) and tailward (rostrocaudal) directions. This, however, may not be the case because in the PLL of larval zebrafish mechanotransduction by rostrocaudal-tuned hair cells is predominantly dependent on Tmc2b function, whereas caudorostral-tuned hair cells use a combination of Tmc2a and Tmc2b⁶². This heterogeneity has not yet been found to be transduced into differential LAN activity, and its relevance for rheotaxis remains untested. Also, our circuit model does not incorporate the efferent

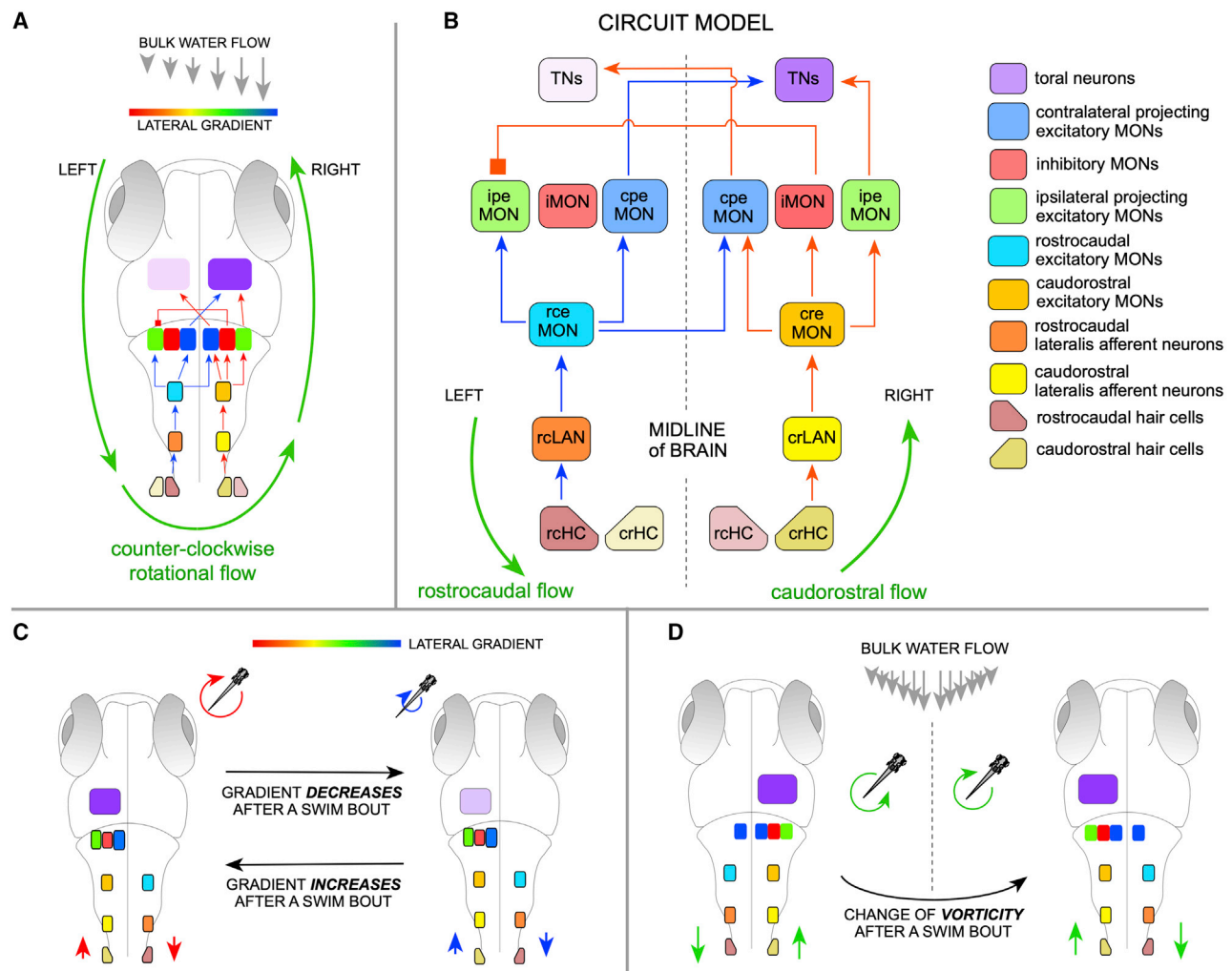


Figure 5. Model circuit of rheotaxis

(A) Two-dimensional scheme of the model circuit represented within a larval zebrafish. Rotational flow (counter-clockwise) is represented by green circular arrows. A gradient of flow velocity is represented as a rainbow bar assigning the highest water-velocity gradient in red, and the lowest in blue. Here, only the positively stimulated HCs and LANs are shown.

(B) The model circuit with transmission of rostrocaudal flow (represented as blue arrows within) and caudostral flow (red arrows within). Inter-hemispheric activity differences upon rotational flow and cross-hemispheric inhibition break symmetry of the system and solve vectorial ambiguity. Acronyms are spelled out on the right.

(C) Top view of larval zebrafish performing rheotaxis under laminar water flow. A gradient of flow velocity is represented as a rainbow bar. As the fish swims in bouts across the horizontal plane, it will experience a decrease (red-to-blue transition) or increase (blue-to-red transition) in the magnitude of the rotational flow, which is directly linked to the gradient of bulk water flow. If gradient increases or decreases, the neuronal activity in the TNs will change (intensity differences in lilac) regardless of vorticity handedness. For simplicity, and because the system is lateral symmetric, only the active cells are depicted.

(D) If the direction of rotation of local flow reverses when animals cross the midline of the water column (or experiences reversal of rotation flow upon its own directional changes across the horizontal plane), the system would simply undergo a mirror symmetric reversal of information reaching the brain.

See also Figure S5.

system. In the larval zebrafish lateral line, efferent input can have a strong inhibitory effect on the release of glutamate at the hair cell-LAN synapse⁶³. Efferent input has been found to be asymmetric, in that selectively acts on rostrocaudal-tuned hair cells. The efferent system is primarily active during swimming bouts, rather than in the interbout during which local rotational flow is detected to determine flow direction. Therefore, it remains unclear if a direction-biased efferent system plays a significant role during rheotaxis under laminar water currents. Nevertheless, future work

should take into consideration these peripheral asymmetries as it is conceivable that the lateral-line system uses peripheral asymmetries in conjunction with lateralized information flow to improve the determination of changes in vorticity.

Conclusion

Our findings reveal three general principles of the mechanism that underlies rheotaxis. First, that mechanical cues detected locally by spatially distributed receptors converge as they are

transmitted to the brain, supporting the conclusion that that PLL acts as a consolidated unit. Second, that opposing directions of water flow on either side of the fish are processed in parallel in the hindbrain. Third, that inter-hemispheric unequal representation of headward and tailward flow breaks the inherent symmetry of the lateral-line system to enable the determination of water flow direction without an external references frame. Finally, our circuit supports an implicit condition of the behavioral algorithm⁵ – the existence of a curl-detecting module in a higher brain area that is transiently activated exclusively upon asymmetric TN activity, allowing the comparison of vorticity between consecutive interbouts. Our model predicts that this module does not respond directly to flow direction, but to interhemispheric differences of toral neuron activity. This, it is likely located in the optic tectum or the telencephalon^{61,64}. The circuit architecture that we propose has been purposely generated to be the most parsimonious that unifies all available data. As such, we assume that it is inherently incomplete. Therefore, future work should assess functional connectivity among candidate neurons and identify additional components.

STAR★METHODS

Detailed methods are provided in the online version of this paper and include the following:

- **KEY RESOURCES TABLE**
- **RESOURCE AVAILABILITY**
 - Lead contact
 - Materials and Availability
 - Data and Code Availability
- **EXPERIMENTAL MODEL AND SUBJECT DETAILS**
 - Ethics statement
 - Fish lines and husbandry
- **METHOD DETAILS**
 - Morpho-anatomical study
 - Functional study
 - Acquisition of the reference brain stack
 - Behavioral assay
- **QUANTIFICATION AND STATISTICAL ANALYSIS**
 - Morpho-anatomical study
 - Functional study
 - Anatomical registration
 - Behavioral assay

SUPPLEMENTAL INFORMATION

Supplemental Information can be found online at <https://doi.org/10.1016/j.cub.2021.01.045>.

ACKNOWLEDGMENTS

We thank Dr. A. Miguel Fernandes (MPI Munich) for advice on the mapZebbrain atlas. This research was supported by NIH grant R01NS39600 to G.A.A., the Max-Planck Society to R.P., and NIH BRAIN Initiative grant 1U19NS104653-01, BMBF grant 01GQ1904, and the Helmholtz Association to H.L.-S.

AUTHOR CONTRIBUTIONS

H.L.-S. conceived the project. G.V., D.A.M., A.A., and J.-P.B. conducted experiments, generated, and analyzed data. K.B., O.R., G.A.A., R.P., and

H.L.-S. analyzed data. H.L.-S. acquired funding. G.V. wrote the first draft of the manuscript. All authors reviewed and approved the final version of the manuscript.

DECLARATION OF INTERESTS

The authors declare no competing interests.

Received: August 14, 2019

Revised: November 30, 2020

Accepted: January 13, 2021

Published: February 4, 2021

REFERENCES

1. Robie, A.A., Hirokawa, J., Edwards, A.W., Umayam, L.A., Lee, A., Phillips, M.L., Card, G.M., Korff, W., Rubin, G.M., Simpson, J.H., et al. (2017). Mapping the neural substrates of behavior. *Cell* 170, 393–406 e28.
2. López, C. (2016). The vestibular system: balancing more than just the body. *Curr. Opin. Neurol.* 29, 74–83.
3. Montgomery, J., Baker, C.F., and Carton, A.G. (1997). The lateral line can mediate rheotaxis in fish. *Nature* 389, 960–963.
4. Olive, R., Wolf, S., Dubreuil, A., Bormuth, V., Debrégeas, G., and Candelier, R. (2016). Rheotaxis of larval zebrafish: behavioral study of a multi-sensory process. *Front. Syst. Neurosci.* 10, 14.
5. Oteiza, P., Odstrcil, I., Lauder, G., Portugués, R., and Engert, F. (2017). A novel mechanism for mechanosensory-based rheotaxis in larval zebrafish. *Nature* 547, 445–448.
6. Seemungal, B.M., Glasauer, S., Gresty, M.A., and Bronstein, A.M. (2007). Vestibular perception and navigation in the congenitally blind. *J. Neurophysiol.* 97, 4341–4356.
7. Kulpa, M., Bak-Coleman, J., and Coombs, S. (2015). The lateral line is necessary for blind cavefish rheotaxis in non-uniform flow. *J. Exp. Biol.* 218, 1603–1612.
8. Chagnaud, B.P., Brücker, C., Hofmann, M.H., and Bleckmann, H. (2008). Measuring flow velocity and flow direction by spatial and temporal analysis of flow fluctuations. *J. Neurosci.* 28, 4479–4487.
9. Engelmann, J., Hanke, W., Mogdans, J., and Bleckmann, H. (2000). Hydrodynamic stimuli and the fish lateral line. *Nature* 408, 51–52.
10. Ghysen, A., and Dambly-Chaudière, C. (2007). The lateral line microcosmos. *Genes Dev.* 21, 2118–2130.
11. López-Schier, H., and Hudspeth, A.J. (2006). A two-step mechanism underlies the planar polarization of regenerating sensory hair cells. *Proc. Natl. Acad. Sci. USA* 103, 18615–18620.
12. Pujol-Martí, J., and López-Schier, H. (2013). Developmental and architectural principles of the lateral-line neural map. *Front. Neural Circuits* 7, 47.
13. Faucher, A., Pujol-Martí, J., Kawakami, K., and López-Schier, H. (2009). Afferent neurons of the zebrafish lateral line are strict selectors of hair-cell orientation. *PLoS ONE* 4, e4477.
14. Haehnel-Taguchi, M., Akanyeti, O., and Liao, J.C. (2014). Afferent and motoneuron activity in response to single neuromast stimulation in the posterior lateral line of larval zebrafish. *J. Neurophysiol.* 112, 1329–1339.
15. Nagiel, A., Andor-Ardó, D., and Hudspeth, A.J. (2008). Specificity of afferent synapses onto plane-polarized hair cells in the posterior lateral line of the zebrafish. *J. Neurosci.* 28, 8442–8453.
16. Raible, D.W., and Kruse, G.J. (2000). Organization of the lateral line system in embryonic zebrafish. *J. Comp. Neurol.* 421, 189–198.
17. Liao, J.C., and Haehnel, M. (2012). Physiology of afferent neurons in larval zebrafish provides a functional framework for lateral line somatotopy. *J. Neurophysiol.* 107, 2615–2623.
18. Lozano-Ortega, M., Valera, G., Xiao, Y., Faucher, A., and López-Schier, H. (2018). Hair cell identity establishes labeled lines of directional mechanosensation. *PLoS Biol.* 16, e2004404.

19. Pujol-Martí, J., Zecca, A., Baudoin, J.P., Faucherre, A., Asakawa, K., Kawakami, K., and López-Schier, H. (2012). Neuronal birth order identifies a dimorphic sensorineural map. *J. Neurosci.* 32, 2976–2987.
20. Trapani, J.G., and Nicolson, T. (2010). Physiological recordings from zebrafish lateral-line hair cells and afferent neurons. *Methods Cell Biol.* 100, 219–231.
21. van Netten, S., and McHenry, M.J. (2014). The Biophysics of the Fish Lateral Line. In *The Lateral Line: Springer Handbook of Auditory Research, Vol. 48*, S. Coombs, H. Bleckmann, R.R. Fay, and A.N. Popper, eds. (Springer).
22. Coombs, S. (2001). Smart skins: information processing by lateral line flow sensors. *Auton. Robots* 17, 255–261.
23. Lyon, E.P. (1904). On rheotropism. I. Rheotropism in fishes. *Am. J. Physiol.* 12, 149–161.
24. Parker, G.H. (1904). The function of the lateral-line organs in fishes. *Bull U S Fish Comm* 22, 45–64.
25. Miyasaka, N., Arganda-Carreras, I., Wakisaka, N., Masuda, M., Sümbül, U., Seung, H.S., and Yoshihara, Y. (2014). Olfactory projectome in the zebrafish forebrain revealed by genetic single-neuron labelling. *Nat. Commun.* 5, 3639.
26. Ohyama, T., Schneider-Mizell, C.M., Fetter, R.D., Aleman, J.V., Franconville, R., Rivera-Alba, M., Mensh, B.D., Branson, K.M., Simpson, J.H., Truman, J.W., et al. (2015). A multilevel multimodal circuit enhances action selection in *Drosophila*. *Nature* 520, 633–639.
27. Tay, T.L., Ronneberger, O., Ryu, S., Nitschke, R., and Driever, W. (2011). Comprehensive catecholaminergic projectome analysis reveals single-neuron integration of zebrafish ascending and descending dopaminergic systems. *Nat. Commun.* 2, 171.
28. Kunst, M., Laurell, E., Mokayes, N., Kramer, A., Kubo, F., Fernandes, A.M., Förster, D., Dal Maschio, M., and Baier, H. (2019). A cellular-resolution atlas of the larval zebrafish brain. *Neuron* 103, 21–38.e5.
29. Wanner, A.A., Genoud, C., Masudi, T., Siksou, L., and Friedrich, R.W. (2016). Dense EM-based reconstruction of the interglomerular projectome in the zebrafish olfactory bulb. *Nat. Neurosci.* 19, 816–825.
30. Bargmann, C.I., and Marder, E. (2013). From the connectome to brain function. *Nat. Methods* 10, 483–490.
31. Engert, F. (2014). The big data problem: turning maps into knowledge. *Neuron* 83, 1246–1248.
32. Kindt, K.S., Finch, G., and Nicolson, T. (2012). Kinocilia mediate mechanosensitivity in developing zebrafish hair cells. *Dev. Cell* 23, 329–341.
33. Randlett, O., Wee, C.L., Naumann, E.A., Nnaemeka, O., Schoppik, D., Fitzgerald, J.E., Portugues, R., Lacoste, A.M., Riegler, C., Engert, F., and Schier, A.F. (2015). Whole-brain activity mapping onto a zebrafish brain atlas. *Nat. Methods* 12, 1039–1046.
34. Ahrens, M.B., Li, J.M., Orger, M.B., Robson, D.N., Schier, A.F., Engert, F., and Portugues, R. (2012). Brain-wide neuronal dynamics during motor adaptation in zebrafish. *Nature* 485, 471–477.
35. Chen, X., Mu, Y., Hu, Y., Kuan, A.T., Nikitchenko, M., Randlett, O., Chen, A.B., Gavornik, J.P., Sompolsky, H., Engert, F., et al. (2018). Brain-wide organization of neuronal activity and convergent sensorimotor transformations in larval zebrafish. *Neuron* 100, 876–890.e5.
36. Hildebrand, D.G.C., Cicconet, M., Torres, R.M., Choi, W., Quan, T.M., Moon, J., Wetzel, A.W., Scott Champion, A., Graham, B.J., Randlett, O., et al. (2017). Whole-brain serial-section electron microscopy in larval zebrafish. *Nature* 545, 345–349.
37. Jetli, S.K., Vendrell-Llopis, N., and Yaksi, E. (2014). Spontaneous activity governs olfactory representations in spatially organized habenular microcircuits. *Curr. Biol.* 24, 434–439.
38. Naumann, E.A., et al. (2016). From whole-brain data to functional circuit models: the zebrafish optomotor response. *Cell* 167, 947–960.e20.
39. Randlett, O., Haesemeyer, M., Forkin, G., Shoenhard, H., Schier, A.F., Engert, F., and Granato, M. (2019). Distributed plasticity drives visual habituation learning in larval zebrafish. *Curr. Biol.* 29, 1337–1345.e4.
40. Easley-Neal, C., Fierro, J., Jr., Buchanan, J., and Washbourne, P. (2013). Late recruitment of synapsin to nascent synapses is regulated by Cdk5. *Cell Rep.* 3, 1199–1212.
41. Fame, R.M., Brajon, C., and Ghysen, A. (2006). Second-order projection from the posterior lateral line in the early zebrafish brain. *Neural Dev.* 1, 4.
42. Luo, L., and Flanagan, J.G. (2007). Development of continuous and discrete neural maps. *Neuron* 56, 284–300.
43. Pujol-Martí, J., Baudoin, J.P., Faucherre, A., Kawakami, K., and López-Schier, H. (2010). Progressive neurogenesis defines lateralis somatotopy. *Dev. Dyn.* 239, 1919–1930.
44. Pujol-Martí, J., Faucherre, A., Aziz-Bose, R., Asgharsharghi, A., Colombelli, J., Trapani, J.G., and López-Schier, H. (2014). Converging axons collectively initiate and maintain synaptic selectivity in a constantly remodeling sensory organ. *Curr. Biol.* 24, 2968–2974.
45. Miri, A., Daie, K., Burdine, R.D., Aksay, E., and Tank, D.W. (2011). Regression-based identification of behavior-encoding neurons during large-scale optical imaging of neural activity at cellular resolution. *J. Neurophysiol.* 105, 964–980.
46. Portugues, R., Feierstein, C.E., Engert, F., and Orger, M.B. (2014). Whole-brain activity maps reveal stereotyped, distributed networks for visuomotor behavior. *Neuron* 81, 1328–1343.
47. Coombs, S., Mogdans, J., Halstead, M., and Montgomery, J. (1998). Transformation of peripheral inputs by the first-order lateral line brainstem nucleus. *J. Comp. Physiol. A Neuroethol. Sens. Neural Behav. Physiol.* 182, 606–626.
48. New, J.G., Coombs, S., McCormick, C.A., and Oshel, P.E. (1996). Cytoarchitecture of the medial octavolateralis nucleus in the goldfish, *Carassius auratus*. *J. Comp. Neurol.* 366, 534–546.
49. Finger, T.E., and Tong, S.L. (1984). Central organization of eighth nerve and mechanosensory lateral line systems in the brainstem of ictalurid catfish. *J. Comp. Neurol.* 229, 129–151.
50. Boord, R.L., and McCormick, C.A. (1984). Central lateral line and auditory pathways: a phylogenetic perspective. *Am. Zool.* 24, 765–774.
51. Wullmann, M.F., and Grothe, B. (2013). The central nervous organization of the lateral line system. S. Coombs, H. Bleckmann, R. Fay, and A. Popper, eds. (Springer), pp. 195–251.
52. Mikami, Y., Yoshida, T., Matsuda, N., and Mishina, M. (2004). Expression of zebrafish glutamate receptor delta2 in neurons with cerebellum-like wiring. *Biochem. Biophys. Res. Commun.* 322, 168–176.
53. Sassa, T., Aizawa, H., and Okamoto, H. (2007). Visualization of two distinct classes of neurons by gad2 and zic1 promoter/enhancer elements in the dorsal hindbrain of developing zebrafish reveals neuronal connectivity related to the auditory and lateral line systems. *Dev. Dyn.* 236, 706–718.
54. Russell, I.J. (1976). Central inhibition of lateral line input in the medulla of the goldfish by neurones which control active body movements. *J. Comp. Physiol.* 111, 335–358.
55. Satou, C., Kimura, Y., Hirata, H., Suster, M.L., Kawakami, K., and Higashijima, S. (2013). Transgenic tools to characterize neuronal properties of discrete populations of zebrafish neurons. *Development* 140, 3927–3931.
56. Kröther, S., Mogdans, J., and Bleckmann, H. (2002). Brainstem lateral line responses to sinusoidal wave stimuli in still and running water. *J. Exp. Biol.* 205, 1471–1484.
57. Plachta, D.T., Hanke, W., and Bleckmann, H. (2003). A hydrodynamic topographic map in the midbrain of goldfish *Carassius auratus*. *J. Exp. Biol.* 206, 3479–3486.
58. Bleckmann, H. (2004). 3-D-orientation with the octavolateralis system. *J. Physiol. Paris* 98, 53–65.
59. Thompson, A.W., Vanwalleghem, G.C., Heap, L.A., and Scott, E.K. (2016). Functional profiles of visual-, auditory-, and water flow-responsive neurons in the zebrafish tectum. *Curr. Biol.* 26, 743–754.
60. Reinig, S., Driever, W., and Arrenberg, A.B. (2017). The descending diencephalic dopamine system is tuned to sensory stimuli. *Curr. Biol.* 27, 318–333.

61. Vanwalleghe, G., Schuster, K., Taylor, M.A., Favre-Bulle, I.A., and Scott, E.K. (2020). Brain-wide mapping of water flow perception in zebrafish. *J. Neurosci.* **40**, 4130–4144.
62. Chou, S.W., Chen, Z., Zhu, S., Davis, R.W., Hu, J., Liu, L., Fernando, C.A., Kindig, K., Brown, W.C., Stepanyan, R., and McDermott, B.M., Jr. (2017). A molecular basis for water motion detection by the mechanosensory lateral line of zebrafish. *Nat. Commun.* **8**, 2234.
63. Pichler, P., and Lagnado, L. (2020). Motor Behavior Selectively Inhibits Hair Cells Activated by Forward Motion in the Lateral Line of Zebrafish. *Curr. Biol.* **30**, 150–157.e3.
64. Finger, T.E. (1980). Nonolfactory sensory pathway to the telencephalon in a teleost fish. *Science* **210**, 671–673.
65. Kim, D.H., Kim, J., Marques, J.C., Grama, A., Hildebrand, D.G.C., Gu, W., Li, J.M., and Robson, D.N. (2017). Pan-neuronal calcium imaging with cellular resolution in freely swimming zebrafish. *Nat. Methods* **14**, 1107–1114.
66. Schindelin, J., Arganda-Carreras, I., Frise, E., Kaynig, V., Longair, M., Pietzsch, T., Preibisch, S., Rueden, C., Saalfeld, S., Schmid, B., et al. (2012). Fiji: an open-source platform for biological-image analysis. *Nat. Methods* **9**, 676–682.
67. Ascoli, G.A., Maraver, P., Nanda, S., Polavaram, S., and Armañanzas, R. (2017). Win-win data sharing in neuroscience. *Nat. Methods* **14**, 112–116.
68. Scorcioni, R., Polavaram, S., and Ascoli, G.A. (2008). L-Measure: a web-accessible tool for the analysis, comparison and search of digital reconstructions of neuronal morphologies. *Nat. Protoc.* **3**, 866–876.
69. Li, Y., Wang, D., Ascoli, G.A., Mitra, P., and Wang, Y. (2017). Metrics for comparing neuronal tree shapes based on persistent homology. *PLoS ONE* **12**, e0182184.
70. Nanda, S., Chen, H., Das, R., Bhattacharjee, S., Cuntz, H., Torben-Nielsen, B., Peng, H., Cox, D.N., De Schutter, E., and Ascoli, G.A. (2018). Design and implementation of multi-signal and time-varying neural reconstructions. *Sci. Data* **5**, 170207.
71. Kist, A.M., Knogler, L.D., Markov, D.A., Yildizoglu, T., and Ruben Portugues, R. (2017). Whole-Brain Imaging Using Genetically Encoded Activity Sensors in Vertebrates. In *Decoding Neural Circuit Structure and Function*, A. Celik, and M.F. Wernet, eds. (Springer), pp. 321–341.

STAR★METHODS

KEY RESOURCES TABLE

REAGENT or RESOURCE	SOURCE	IDENTIFIER
Antibodies		
p-ERK antibody	Cell Signaling	Cat. No. #4370
t-ERK antibody	Cell Signaling	Cat. No. #4696
Bacterial and Virus Strains		
Biological Samples		N/A
Chemicals, Peptides, and Recombinant Proteins		
Tricaine (MS-222)	PHARMAQ	Cat#QN01A X93
Red dextran (Tetramethylrhodamine, 3000 MW)	Invitrogen	ref.D3308
Magenta dextran (Alexa Fluor 647, 10000 MW)	Invitrogen	ref.D22914
Polychromatic Red Microspheres	Polysciences	Cat#19507
Alpha-bungarotoxin	Cayman Scientific	Cat#16385
Experimental Models: Organisms/Strains		
Zebrafish: Tg[myo6b:β-actin-GFP]	Kindt lab	32
Zebrafish: Tg[HGn39D]	López-Schier lab	13
Zebrafish: Tg[elavl3:GCaMP6s]	Engert lab	65
Zebrafish: Tg[sill:mCherry]	López-Schier lab	2
Recombinant DNA		
hsp70:mCherry-SILL (SILL:mCherry)	López-Schier lab	13
Sill:Gal4-VP16	López-Schier lab	This paper
UAS:Synapsin1-GFP	Washbourne lab	40
Software and Algorithms		
Fiji	https://imagej.nih.gov/ij/index.html	66
Amira (5.3.3)	Thermo Fisher Scientific	N/A
Computational Morphometry Toolkit	https://www.nitrc.org/projects/cmtk/	66
Z-Brain atlas	https://engertlab.fas.harvard.edu/Z-Brain/	33
MapZeBrain atlas	https://fishatlas.neuro.mpg.de	28
Other		
iLas Pulse® laser system	Roper Scientific SAS, France	N/A
Mai Tai Ti:Sapphire laser	Spectra Physics	N/A

RESOURCE AVAILABILITY

Lead contact

H.L.-S. (hernan.lopez-schier@helmholtz-muenchen.de).

Materials and Availability

This study did not generate new unique reagents or transgenic lines. Requests for resources and reagents should be directed to and will be fulfilled by the Lead Contact.

Data and Code Availability

The datasets supporting the current study are available from the corresponding author on request. Neuronal reconstruction (SWC files) will publicly releases on the [NeuroMopho.org](https://neuroMopho.org) site upon acceptance of the paper⁶⁷.

EXPERIMENTAL MODEL AND SUBJECT DETAILS

Ethics statement

Experiments with wild-type and transgenic animals of undetermined sex were conducted under a protocol approved by the Ethical Committee of Animal Experimentation of the Parc de Recerca Biomedica de Barcelona (Spain), and protocol number Gz.:55.2-1-54-2532-202-2014 by the “Regierung von Oberbayern” (Germany).

Fish lines and husbandry

Adult zebrafish (*Danio rerio*) were maintained under standardized conditions. Larvæ were collected from natural spawning and kept in E3 medium in 14/10 h light/dark cycle at 28°C. For the morpho-anatomical study, we used larvæ of a double transgenic line Tg[Myo6b:β-actin-GFP; HGn39D]^{13,32} at 6 days-post-fertilization (dpf). For behavioral assay, we used 5.5 dpf HGn39D larvæ^{5,13}. For functional imaging experiments we used larvæ with pan-neuronal expression of GCaMP6s (Tg[elavl3:GCaMP6s])⁶⁵ at 6 - 7 dpf.

METHOD DETAILS

Morpho-anatomical study

Labeling single lateralis afferent neurons. We labeled single LANs by injection of 20 pg of cDNA of Sill:mCherry¹³ as a plasmid into 2-to-4-cells double Tg[Myo6b:β-actin-GFP; HGn39D] transgenic embryos. The resulting larvæ were anesthetized using bath-applied solution of MS-222 (tricaine) at a concentration of 0.16 g/L and screened at 2-3 dpf with an epifluorescence stereomicroscope (Carl Zeiss, Germany) to select fish with single labeled LANs. To test the correlation between terminal-branch varicosities and synapses, we co-injected 20 pg of Sill:mCherry¹³, Sill:Gal4-VP16¹⁸ and UAS:Synapsin1-GFP⁴⁰ in 2-to-4-cells WT embryos. Larvæ with double fluorescent labeling were selected for live imaging.

Single-cell imaging. Selected specimens (n = 176) were live imaged at 6 dpf under an inverted spinning-disk confocal microscope using a 40x dry objective and excitation at 488nm and 556nm. Fish were anesthetized in bath-applied solution of tricaine (0.16 g/L) and embedded in 1% low melting point agarose. Two partially overlapping z stacks were acquired to cover the central projection and the soma of the LANs. Larvæ used for tracking the development of LAN's central arbors, were live imaged every day from 2.5 to 6.5 dpf (n = 5).

Manual image processing and axonal tracing. Individual LAN's confocal z stacks were processed manually. The two channels of each z stack were merged with Fiji and all pairs of overlapping stacks were stitched using the 3D Stitching Plugin for Fiji selecting coincident ROIs to generate composite images⁶⁸. Subsequent axonal tracing was performed using Amira Software 5.3.3 (Thermo Fisher Scientific). The mCherry channel was used to manually trace each LAN from the center of the soma to the anterior- and posterior- end of the central arbor. This generated artifactual intermediate nodes, which were deleted with the Remove Intermediate Nodes tool. The secondary branches were traced from the central arbor to the distal ends and varicosities were marked as nodes. The “Identify Graphs” tool was run to color-code each branch and their varicosities. These reconstructions were aimed to count varicosities and classify neurons according to the morphology. For the neuronal development study, we traced and reconstructed the LAN's axons by hand with Fiji and the Simple Neurite Tracer plugin⁶⁸.

Microsurgery. Laser microsurgery was used to sever the peripheral projection of lateral-line neurons. It was performed using the iLas Pulse® laser system (Roper Scientific SAS, France) equipped with an ultraviolet laser (355 nm emission) mounted on an inverted microscope Zeiss Axio Observer® equipped with a 63 × water immersion objective lens^{18,44}. Larvæ at 4dpf were anesthetized and embedded in 1% agarose. Peripheral axons were cut between the posterior ganglion and the first neuromast (L1). Multiple laser pulses were repeatedly applied until axons were severed. Distal axon fragment detachment from the neuron was confirmed ~1 h later. The larvæ were then released from the agarose and kept in E3 medium under standard conditions. These specimens were used for analysis 36 h after axon severing. After the behavioral experiments, the specimens were imaged again to certify the presence of intact hair cells in neuromasts.

Neuronal labeling by fluorescent dextrans. To label neurons from pre-selected neuromasts we used anionic, fixable red- fluorescent dextran [tetramethylrhodamine, 3000 MW (molecular weight) (Invitrogen ref. D3308) and magenta-fluorescent dextran (Alexa Fluor 647, 10,000 MW (Invitrogen ref.D22914). Imaging was done one day after dextran injection¹⁹. Only samples with the neuronal labeling specific to individual neuromasts were included in the analysis.

Functional study

Sample preparation. To identify hindbrain areas activated by pLANs of different planar polarity, we performed two-photon calcium imaging in paralyzed larval zebrafish with pan-neuronal expression of GCaMP6s (Tg[elavl3:GCaMP6s])⁶⁵, while stimulating the L3 neuromast in both the caudorostral and rostrocaudal directions. Animals were paralyzed by incubating in bath-applied buffered 1 mg/mL alpha-bungarotoxin (Cayman Scientific, Concord, CA) for 10 min. Cupulæ of neuromasts were labeled by incubating larvæ in a suspension of Fluoresbrite Polychromatic Red Microspheres with a diameter of 0.5 microns (Polysciences, Warrington, PA, 1 droplet per 1 mL of distilled water) for 10 min. Paralyzed animals with labeled neuromasts were mounted using a novel method to head-restrain paralyzed larvæ without damaging trunk neuromasts. A cylinder of 1.5% low melting point agarose was made by filling a thin-walled borosilicate glass tube (outer diameter 2 mm) with agarose using a custom-made syringe piston. A longitudinal channel with a diameter of ~0.6 mm was made in the cylinder by placing a metal rod in the tube before the agarose sets. A small longitudinal

incision was made on the agarose cylinder with a scalpel to enable for the accurate opening of the agarose cylinder with forceps and the placing larvæ inside the cylinder. Larvæ were then placed inside the channel in the agarose cylinder such that the trunk was outside of the agarose and therefore exposed to stimulation. The borosilicate tube filled with agarose holding a mounted larva was secured in a 3D-printed plastic chamber. Mounted larvæ were imaged under a fluorescent stereoscope to ensure that L3 neuromast on the left side of the larva was labeled with microspheres before imaging under a custom-built two-photon microscope.

Single neuromast stimulation. Stimulation of the L3 neuromast was performed under a custom-built two-photon scanning microscope using patch-clamp electrodes for electrophysiological recordings. Electrodes were pulled from thick-walled borosilicate glass with filament and were filled with rhodamine solution for visualization under PMT of the two-photon microscope. Electrodes were oriented along the rostro-caudal axis of larvæ and aimed toward the rostral direction and placed to be in close proximity of the L3 neuromast using a micromanipulator (Sutter Instruments, Novato, CA). The visualization of electrodes and neuromasts was performed using an infrared-sensitive camera (Pike F032B, Allied Vision Technologies) during the initial crude placement (illumination was provided by 850 nm wavelength LEDs) and using the PMT of the two-photon microscope during the final accurate placement. The stimulating electrodes were connected to a pipette that was used to generate positive and negative pressure in the electrode resulting in outward or inward gentle flow from its tip, respectively. Since the electrodes were oriented toward the rostral part of the larvæ, outward flow resulted in a caudorostral (cr) inclination of the neuromast, whereas inward flow resulted in a rostrocaudal (rc) inclination of the L3 neuromast. Stimulation during imaging experiments was performed manually. For 2 out of the 8 analyzed fish we imaged the inclination of neighboring neuromasts (L2 and L4) caused by stimulation and confirmed that its amplitude was very small compared to the amplitude of the L3 inclination (data not shown). The stimulation paradigm consisted of 3 caudorostral stimulation trials and 3 rostrocaudal trials per plane. Each trial was ~ 7.4 s long (10 full frames, see below). Trials were presented in an alternating manner, with caudorostral stimulation being the first on each plane (see below).

Functional imaging data acquisition. A Ti:Sapphire laser (Mai Tai, Spectra Physics, Santa Clara, CA) tuned to 905 nm was used for excitation of GCaMP6s. Larval brains were systematically imaged while performing lateral line stimulation as described above. Full frames were acquired every 736.88 ms in four, ~ 0.76 - μm -spaced interlaced scans, which results in x and y pixel dimensions of ~ 0.76 μm . Exceptionally, in order to acquire responses of the posterior lateral line ganglion (PLLg) ipsilateral to the stimulation side with higher resolution, the spacing of interlaced scans was decreased to ~ 0.34 μm . Imaging stacks were acquired in the dorsal to ventral direction. After all 6 stimuli were presented in one plane, the focal plane was shifted ventrally by 2 μm and the process was repeated. Before and after brain scanning, the effectiveness of stimulation was confirmed by recording responses from the ipsilateral PLLGs. Only larvæ showing response to each stimulation in at least one pLAN underwent whole-brain scanning, and only larvæ showing consistent responses to each stimulation in the same LAN after the brain scanning were included in the analysis.

Acquisition of the reference brain stack

To acquire the reference stack used for anatomical registration of both structural and functional data, an anesthetized 6 dpf *Tg[Huc:GCaMP6s; Sill:mCherry]* larva was mounted in the custom-made chamber used in functional imaging experiments. The chamber allowed for rotation along the rostro-caudal axis. The reference brain was imaged using a two-channel confocal microscope (LSM700, Carl Zeiss, Germany) from two different angles: top view (dorsal-up) and side view (rotated at $\sim 60^\circ$ to the left to better expose the right posterior LL ganglions and their central arbor).

Behavioral assay

The behavioral rig was identical to a previously designed impulse chamber⁵. It consists of a transparent seamless cylindrical Plexiglas® pipe filled with water. The dimensions of the cylinder (2.4 cm inner diameter) enable isosymmetric freedom of movement for larval zebrafish. The rig is formed by a set of 3 pieces of Plexiglas tube screwed to each other, and named as rear, middle and front piece. The middle piece is the imaging area (effective swimming length 15 cm) where larva will be placed by introducing it from the front piece, which facilitates the introduction of the specimens and avoids holes in the pipe that otherwise will result in a shadowing effect. A mesh is placed at either side of the middle piece of the pipe to prevent the animal from abandoning the imaging area, and also to serve as collimator. An array of light-emitting diodes (LEDs, 940 nm wavelength) was placed below and on one side of the pipe to illuminate the behavioral area with infrared light. A high-speed camera (NX4 series, Imaging solution, GmbH) with a recording capacity of 1000 frame-per-second (fps) in full frame (1024x1024 pixel) was positioned above the pipe (~ 1.2 m away) and a mirror was placed on one side of the pipe at 45° , opposite to the LED array. This configuration allows the camera to simultaneously capture images from the top and side of the behavioral area. The camera and the motor that controls the actuator are connected to a PC through a CAN PCI interface card and digital servo drives (Copley Controls, USA). To create laminar water flow, the plunger was pushed by a linear actuator motor (LCA series, SMAC corporation, USA). A soft and flexible diaphragm was attached to the head of the plunger to enable smoothness of movement and to prevent water from leaking. The plunger moves inside the rear set-piece. Back and forth movement of this diaphragm inside creates water flow inside of the tube. The front piece connects the middle piece to a shallow and wide water reservoir (20x20x3 cm³). Since the refraction index of the Plexiglas® and the water are closer to each other and higher than air, their combination with the curvature of the cylindrical pipe will act as a lens, creating an optical distortion that will hide the larva at the edges of the pipe, and will elongate it according to its position inside the pipe. A simple solution to this problem is to place the rig inside a cube filled with water and made of flat Plexiglas®, which corrects the lensing effect. To assess flow laminarity, we

recorded the trace of a water-soluble dye delivered into the pipe through a small hole at the tip of a syringe needle placed in the middle of the water column at one end of the middle piece of the pipe. The velocity distribution (v) of the flow field within a cylinder as a function of distance (r) from the center of the cylinder is given by:

$$(d^2v/dr^2) + 1/r (dv/dr) = -1/\eta (\Delta P/\Delta x)$$

$$\text{and } v = A + Br^2$$

Where A and B are constants to the boundary conditions of the flow. And $\Delta P/\Delta x$ is the pressure gradient. The three-dimensional velocity profile is then

$$[V(r, u, z)]$$

where r, u, z defines the three-dimensional space. The transverse symmetry of the cylinder allows the treatment of the flow in two dimensions: $[V(r, z)]$. At full development, the flow remains constant, and the flow profile will only vary in the radial (r) direction under no-slip conditions – i.e., Since there is no relative movement in the liquid-solid interface at the wall of the tube, the fluid velocity near the boundary approaches to zero but increases toward the center of the pipe. Thus, the flow-velocity profile ($V(r)$) effectively becomes one dimensional:

$$V(r) = V_m [1 - (r^2/R^2)]$$

Where η is viscosity and V_m is the maximum velocity:

$$V = (1/4\eta) (\Delta P/\Delta x) R^2$$

For each experiment one larva was placed inside the rig 30 min prior to the experiment to allow it to adapt to the conditions and explore the area. All experiments were done in the dark to eliminate any visual input. The temperature of the water was continuously maintained at 28°C by heating the laboratory room (~3 m²) using a heater (Fakir 2002 CTF). Fish movement was recorded for 27 s consisting of 4 s prior to flow onset, followed by 23 s during flow at a specific velocity. Water flow was generated alternatively in two directions by pushing or pulling the plunger. Each trial was followed by a pause of 5-10 min with zero current to not bias larval responses to flow. Fish position and orientation in the pipe was recorded by sequences of images through the camera at 200 images/second and saved to a PC by the Motion studio software (Imaging solution, GmbH) for *a posteriori* analysis. To increase the spatial resolution of the imaging system, we placed the optical component of a Zeiss stereomicroscope (Stemi 2000-C with TV adaptor 2/3" c, 0.63x) between the camera and the imaging area. This decreases the field of view to a quarter but considerably improves spatial resolution of the larva. Animal orientation was recorded over time and represent as orientation for all trials.

QUANTIFICATION AND STATISTICAL ANALYSIS

Morpho-anatomical study

Varicosity counting in central arbors. To quantify the spatial distribution of varicosities, we performed an analysis with three increasing levels of regionalization. For the first level, the number of varicosities was counted along the whole length of the central arbor of each neuron. In the second level, central arbors were spatially sub-divided into two (from their natural branch point), and the number of varicosities was counted in each sub-division for each neuron, and called anterior varicosities (AVs) and posterior varicosities (PVs). Lastly, in the third level of analysis, central arbors were sub-divided into 9 equal quadrants (corresponding to the rhombomeric division of the hindbrain), and we counted the number of varicosities in each quadrant for each neuron. To assess statistical significance of observed differences in varicosities counts between neurons innervating different regions of the lateral line, different neuromasts or different directional tuning (and their combinations), we used two-tailed t tests with significance level of 0.01. We applied ANOVA single-factor tests for the multiple comparison of the number of varicosities in pLAN's central arbors of different neuromasts. Scatter diagrams, bar graphs and heatmaps were generated in Excel. To test the correlation between varicosities and synapsis ($n = 6$), we counted varicosities in the red channel and synaptic puncta in the green channel, of the double fluorescent labeled LANs (mCherry, Synapsin1-GFP). To assess statistical significance of observed correlation between varicosities and synaptic puncta, we used two-tailed t tests with significance level of 0.01.

Neuronal classification. All manual reconstructions were converted in the open SWC format^{68–70}. Fourteen diameter-independent geometric features were extracted from every neuron with the L-Measure software⁶⁸, namely: the tree height, width, and depth after re-orientation along principal components; maximum Euclidian and path (geodesic) distances from root to tip; numbers of terminal tips and of tracing points (fragmentation); Contraction (the ratio between Euclidean and geodesic branch length, providing a measure of tortuosity or "wiggleness"); local and branch-to-branch bifurcation angles; total length, centrifugal branch order, partition asymmetry, and fractal dimension. These morphological attributes were normalized for supervised and unsupervised data analysis by subtracting the mean and scaling to unit variance. Unsupervised clustering was performed by Gaussian mixture models (GMMs) as implemented in the Scikit-learn library for the Python programming language. GMMs are a probabilistic approach that only requires as a parameter the desired number of output clusters (components) and automatically determines the optimal grouping of

all data points to each cluster. The algorithm iteratively finds and optimizes the weights that encode the membership possibility of data points in each group. The results were subjected to principal component analysis to facilitate visualization. In supervised classification, all data points are assigned their labels a priori, and the goal is to identify the sets of features that better separate the groups as well as to determine their relative performance. Well-known algorithms for this purpose include logistic regression, K-nearest neighbors, and multilayer perceptrons. To minimize variance and bias, we combined all three of these methods into an ensemble learning meta-algorithm, a strategy that harnesses multiple techniques into a single improved predictive model. The implementation used Scikit-learn under Python, employing Euclidean distance and 7 neighbors for the K-nearest neighbors module and two hidden layers each containing one hundred nodes (neurons) for the perceptron module. A persistence diagram vector was computed from each SWC file. The vectors are compact metric representations of the global distribution of axonal branches as a function of path distance from the root and can be viewed as a mathematically rigorous version of the traditional “Sholl” plots⁶⁹. The null hypothesis conjectures that arc-sine distances of vectors within the same neuronal populations are drawn from the same distribution as arc-sine distances of vectors from different neuronal populations. Statistical differences were assessed using Bonferroni-corrected 1-tailed unpaired t tests and results were graphed using the Python Matplotlib data visualization library. All software code ran on Ryzen 7 1800x eight-core processor with 16 GB of RAM under the Ubuntu 18.04 operating system.

Functional study

Data alignment. Functional imaging analysis was performed with MATLAB (MathWorks, U.S.A.) using custom-written code. To correct for drift, each image frame was aligned, using translation only, to the average image of that z-plane, and consecutive z-planes were aligned to each other with subpixel precision. For each fish, an anatomical stack was computed by summing the fluorescence across time frames.

Data segmentation. Aligned data were segmented into regions of interest (ROIs) using voxel-wise correlation⁷¹. Briefly, a correlation map was computed, where each voxel brightness equaled to the correlation between the fluorescence time-trace of that voxel and the average trace of 26 adjacent pixels, including voxels from the previous and from the next planes. This ensured that bright regions of the correlation map highlight areas with activity that is consistent across planes, which is therefore likely to result from LL stimulation. The correlation map was segmented into ROIs with the following iterative procedure. Growing of each ROI was initiated from the brightest voxel in the correlation map among the ones still unassigned to ROIs (seed). Adjacent voxels were then gradually added to the growing ROI if eligible for inclusion. Criteria for inclusion were the following: 1) voxel's brightness on the correlation map must be greater than the seed's brightness divided by two; 2) voxel's distance from the seed must be less than 5 μm ; 3) correlation of the voxel's fluorescent trace with the seed's trace must exceed 0.5. Additional criteria for minimal ROI volume ($10 \mu\text{m}^3$) was introduced to remove very small ROIs and to ensure that the ROIs matched approximately the size of neuron somata. In addition, ROIs that were located in only one plane were removed. After segmentation, the fluorescence time-trace of each ROI was extracted by summing fluorescence of all voxels that were assigned to that ROI during segmentation. Each trace was then z-scored on a plane-by-plane basis. Finally, to compare spatial distribution of detected ROIs across animals, all ROIs were registered to a common reference brain (see Anatomical registration).

Identification of direction-selective responses. ROIs with consistent responses to a single neuromast stimulation (regardless of its direction) were identified using the following bootstrapping procedure. We first computed the summed variance across planes for each ROI. Since the stimulation protocol was the same for each imaging plane, ROIs with consistent responses should have small variance. We formulated a null hypothesis for each ROI, that observed activity was not related to the stimulation. To build the corresponding null-distribution of variance, each trace was divided into 6-frame segments, the segments were randomly shuffled 1000 times, and for each iteration, the variance across planes was computed. If the variance of the non-shuffled trace was less than the 5th percentile of the null-distribution (one-tailed alternative with 95% significance level), the ROI was referred to as being responsive and kept for further analysis. To identify ROIs with direction-selective responses, we performed fast Fourier transformation on the traces and computed the phase of the frequency component corresponding to the frequency of stimulation (0.068 Hz). Since the phase followed a bimodal distribution, we divided all ROIs into cr- and rc-selective ROIs using k-means clustering of the phase. To present anatomical location of cr and rc ROIs, we constructed cr and rc binary maps for each fish. Each map was blurred with a three-dimensional Gaussian filter (1 μm standard deviation), and the maps were summed across animals. Therefore, a voxel's brightness on the final map represents number of larvae with respective ROIs in that voxel (Figures 4D and 4H). To identify brain regions with responses to cr or rc stimulation, that are consistent across fish, we formulated the following null-hypothesis for each voxel of the reference brain. If this voxel contained a responsive ROI, this ROI was equally likely to be cr- or rc-selective. We then computed the probability of observing the preference we do (or more extreme preference) if both preferences are equally likely. For example, if a voxel contained a responsive ROI in 7 larvae, and 6 of them are cr-selective, we compute the probability of observing 6 or 7 cr ROIs out of 7 responsive ROIs. If this probability was less than 5%, the null hypothesis of equal probability was rejected and that voxel was referred to as having consistent directional preference across animals. These consistent voxels are presented as three-dimensional renders that were constructed using FIJI 3D viewer plugin⁶⁶.

Registration of Gad1b and calcium signal. To identify whether inhibitory neuronal populations react to unilateral cr- or rc-stimulation of the lateral line, we registered the Gad1b-GFP stack from the Z Brain Atlas to the reference brain (see Anatomical registration). We then manually created a binary mask containing bright voxels of the Gad1b-GFP stack that are located in the MON and computed number of cr- and rc-reactive voxels overlapping with this mask.

Anatomical registration

To represent single-labeled neurons and functional data in the same reference space, acquired images were registered to a single reference brain stack using the free Computational Morphometry Toolkit (CMTK; <http://www.nitrc.org/projects/cmtk/>).

An affine transformation between side and top view reference (side-to-top transformation) was computed using CMTK. In addition, to visualize the results in the context of the whole larval zebrafish brain, the averaged anatomical stack of the larval zebrafish brain⁴³ was registered to top view and side view references. Registration of the single-labeled cells was performed in three steps. First, HGn39D:GFP channels of one posterior ganglion and one anterior ganglion were chosen as the intermediate reference stacks; and affine volume transformations were computed to align all other GFP channels to their respective intermediate reference (anterior or posterior). These transformations were then applied to align single-cell Sill:mCherry channels from each animal. The axons of the registered single-labeled cells were then traced by hand and morphologically reconstructed in three dimensions using the Simple Neurite Tracer plugin for Fiji. To allow for comparison of anatomical properties of posterior and anterior ganglion cells, the affine volume transformations between the intermediate references and the mCherry channel of the final side-view reference were computed. These transformations were then applied to morphological reconstructions of single-labeled cells to align them to the side-view reference brain. Finally, these registered stacks were aligned from the final side-view to the final top-view coordinate space using the side-to-top transformation. For the functional imaging, affine volume transformations were computed to align the anatomical stacks of imaged larvae to the top-view reference. These transformations were then applied to each ROI to identify its coordinates in the reference space. For the registration of the Gad1b expression pattern, the affine volume transformation between the HuC-GCaMP5G stack from Z Brain Atlas³⁵ and the top view of the reference brain was computed. This transformation was then applied to the Gad1b-GFP stack from the Z Brain Atlas.

Behavioral assay

We define a rheotaxis index as the orientation of the larva with respect to the direction of water flow. Positive rheotaxis occurs when the specimen orients by facing the flow. Zero degree when larvae perfectly face the flow and 180 degree when they perfectly orient against the flow. We calculated the cosine of the orientation (trigonometric function, e.g., $\cos(0) = 1$, $\cos(\pm\pi/2) = 0$, $\cos(\pi) = -1$), making the range of behavioral reaction to flow from -1 (negative rheotaxis) to $+1$ (positive rheotaxis). We created a scoring system to describe where larvae perform better rheotaxis by means of orientation to flow. We defined an empty two-dimensional matrix with the same size of the pipe's length and width to assign values of the orientation of the fish at each position in the pipe. The values of the matrix are normalized to a range of values between 0 and 1. The recorded data were fed into Bonsai for extracting the position and the orientation of the animal. Background signal was subtracted from all the images by adaptive thresholding. Closed-ellipse morphological transformation to define animal body shape. By finding the contours of the binary image and analyzing its structure, the posture of the larva was assigned to a two-dimensional Cartesian space for the side and top views of the animal. The orientation of the animal was calculated by finding the major and minor axes of the ellipse. The measured parameters were exported into MATLAB® (MathWorks Inc.) for analysis. Statistical analyses were done with the statistics software R (version 3.3.2) (<https://www.R-project.org/>). For analysis of rheotaxis, Kolmogorov-Smirnov tests and F-tests were employed to check the assumptions for the analyses of variance used to compare the different conditions. The assumptions of normal distribution and homogeneous variance were rejected for some groups, so instead of a one-way analysis of variance we used a Kruskal-Wallis test (also referred to as Kruskal-Wallis one-way analysis of variance by ranks) for the overall comparison of all groups and post hoc tests according to Dunn for pairwise multiple comparisons.

Current Biology, Volume 31

Supplemental Information

A neuronal blueprint for directional mechanosensation in larval zebrafish

Gema Valera, Daniil A. Markov, Kayvan Bijari, Owen Randlett, Amir Asgharsharghi, Jean-Pierre Baudoin, Giorgio A. Ascoli, Ruben Portugues, and Hernán López-Schier

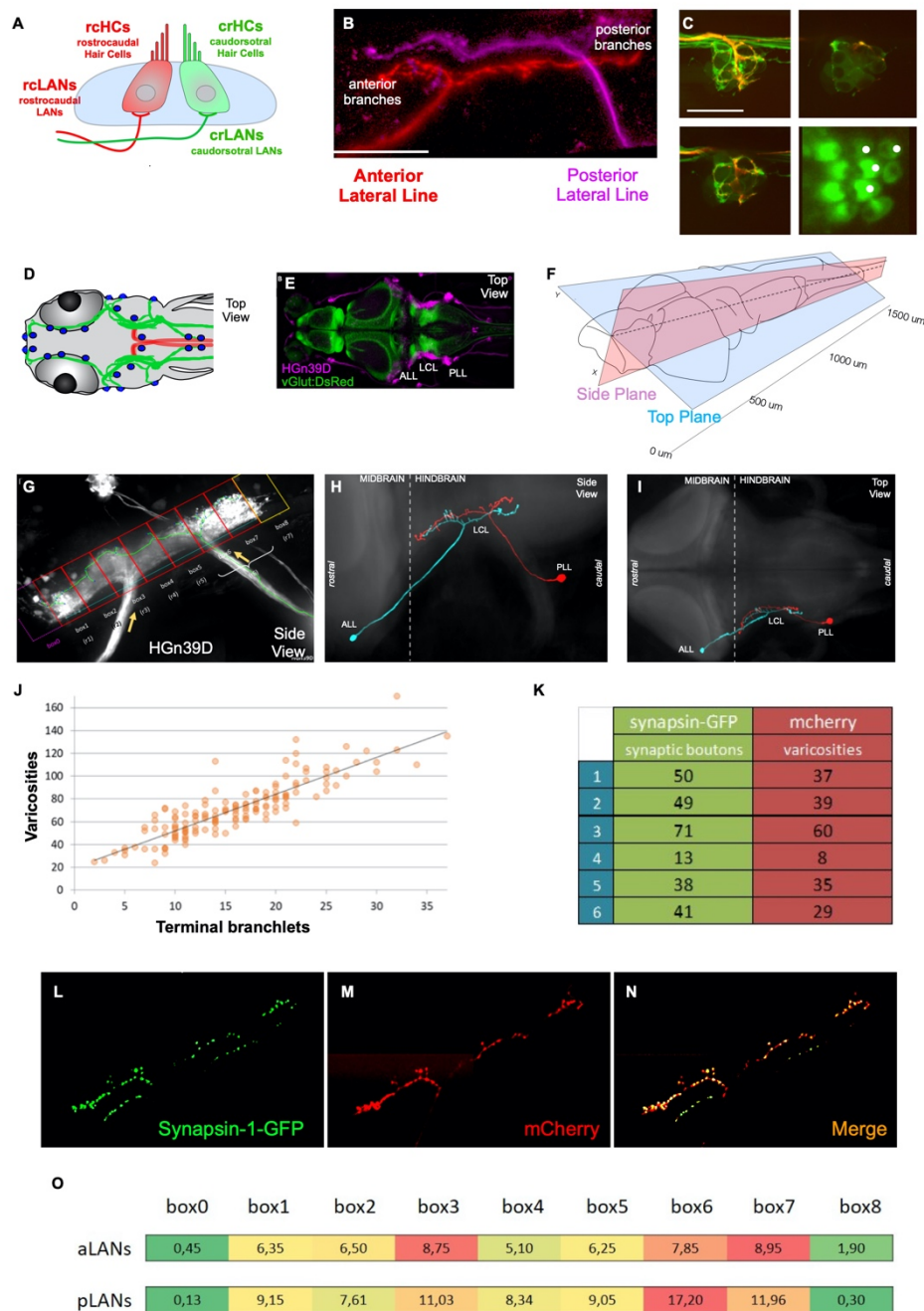


Figure S1. Lateral-line structure. Related to Figure 1. (A) Side view of a neuromast showing planar polarization of hair cells: rostrocaudal-oriented (rcHCs in red) and caudorostral-oriented (crHCs in green). rc-tuned and cr-tuned LANs are also depicted. (B) Confocal image of a larval zebrafish hindbrain highlighting the gross somatotopic organization of aLANs and pLANs central projections. A neuromast of the anterior lateral line (ALL) and one of the PLL were injected,

respectively, with red and magenta dextran, which are transported to the brain by the corresponding LANs. The anterior and posterior branches of LAN central projections are indicated. **(C)** Maximal projection of a confocal series of a horizontal neuromast innervated by a singly-labeled LAN (red) and the entire LAN population (green). Individual optical sections reveal the peripheral arborization of the neuron at the basal and medial domains. The apical domain shows the planar polarization of hair cells, and white dots indicate the hair cells innervated by the marked neuron. **(D)** Scheme of the top view of the lateral-line system in the head of a zebrafish larva. LANs are shown in green. For reference, the reticulospinal Mauthner cells and their axons are in red and the neuromasts are represented as blue circles. **(E)** Top view of the maximal projection of the head of zebrafish larva in the double transgenic line *Tg[HGn39D ; vGlut:DsRed]* (respectively, magenta and green). The posterior (PLL) and anterior (ALL) lateralis ganglia and the lateralis central lintel (LCL) are indicated on the left hemisphere of the brain. **(F)** Scheme indicating the two orthogonal visualization planes with coordinates and indicative distances along the horizontal plane (side plane in pink and top plane in light blue). **(G)** Scheme of the “Box Method” showing the grid of 9 identical boxes. Below each box the rhombomere that approximately corresponds to the box is indicated. Yellow arrows indicate the points of entry of the axons of the ALL and PLL (respectively, approximately in rhombomeres 3 and 6). A single skeletonized pLAN (green) is superimposed to the transgenic line HGn39D (gray). **(H-I)** Volume-filled skeletons of one aLAN (cyan) and one pLAN (red) morphed on a reference brain (gray). **(H)** Side view and **(I)** top view. Both LANs project their central axons towards the LCL in the hindbrain. **(J)** Scatter diagram of terminal branches against varicosities, revealing a linear correlation between these parameters. **(K)** Table with the quantification of the number of varicosities and secondary branches in Synapsin-1-labeled LANs (green) and mCherry-labeled LANs (red) (N = 6). **(L-N)** Side views of the maximal projection of a pLAN co-expressing the presynaptic marker Sill:Synapsin-1-GFP (green in C) and Sill:mCherry (red in D). **(E)** shows the merging of both fluorophores. **(O)** Distribution of varicosities along the central arbor is similar between aLANs (above) and pLANs (below). aLANs show two peaks of high content of varicosities in box 3 and boxes 6-7 respectively. pLANs show one peak in boxes 6-7 and one less pronounced in box 3. Boxes are colored in a green-to-red scale from less to more varicosities. **(P)** Distribution of varicosities in

Ter_pLANs showing that Ter_rcpLANs (blue) have more varicosities than Ter_crpLANs (red). The difference in the number of varicosities is significant in box 1, 5 and 7 (p-values, respectively: 0.00508, 0.00666 and 0.00103; $\alpha = 0.01$).

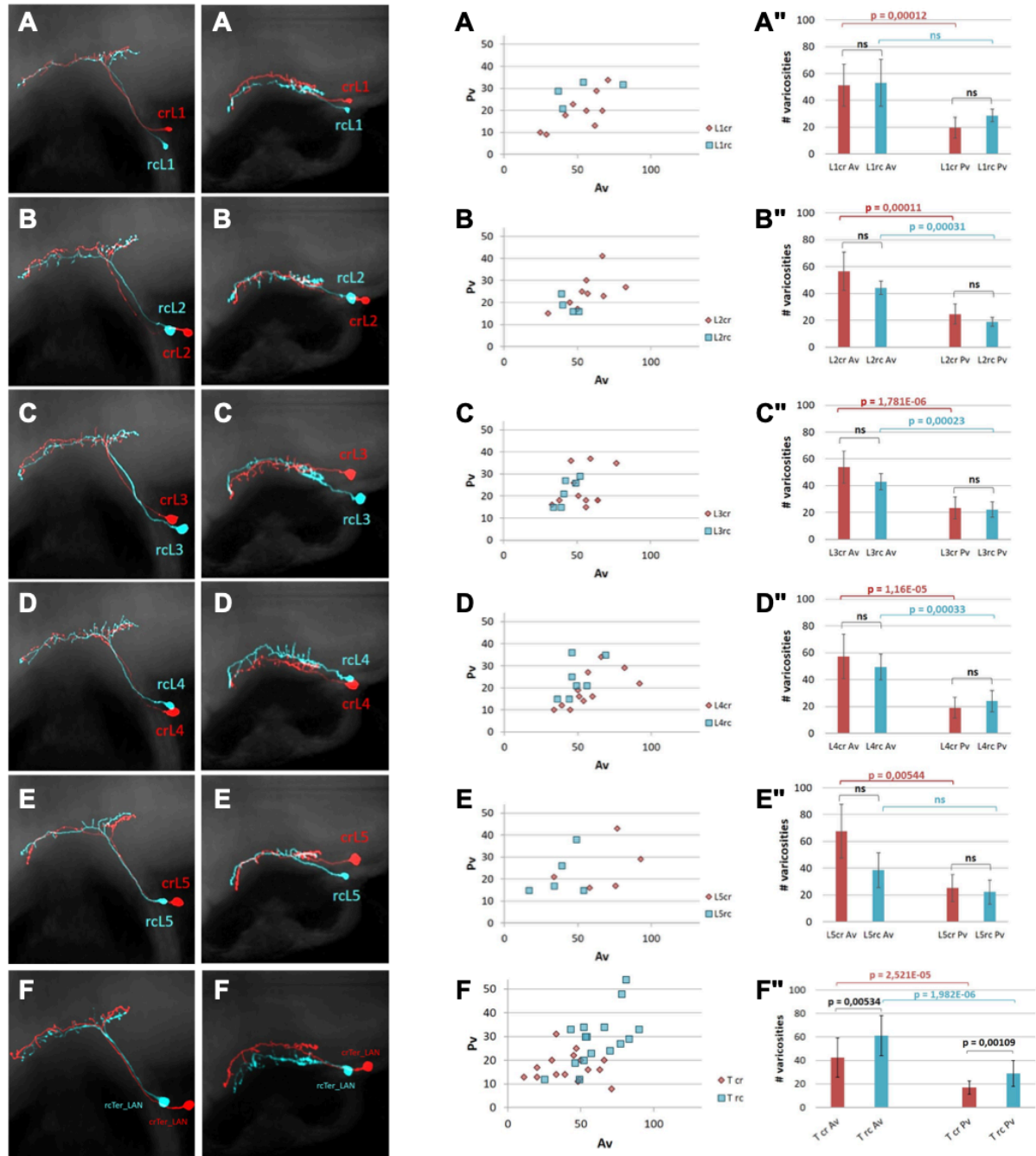


Figure S2. Anatomical characterization of lateralis afferent neurons. Related to Figure 2. (A-E) Side view of pairs of volume-filled skeletons of troncal LANS morphed onto a reference brain. They represent one L1-L5_crpLAN (red) and one L1-L5_rcpLAN (blue) clustered in separated groups from L1 to L5. (A'-E') Top view of the same neurons. Each row (A-F) represents a different level (L1-L5) and compares crpLANs (red) and rcpLANs (blue). Panels A'-F' include bar graphs of the number of varicosities for each group, with p-values indicating significant differences.

of the skeletons of (A-E). (**A''-E''**) crpLANs (red) and rcpLANs (blue) of the trunk of the fish (L1-L5) do not constitute clearly distinguishable morphological classes with respect to the number of AVs and PVs. (**A'''-E'''**) Bar graphs comparing the number of AVs (left) and PVs (right) between separated groups of L1-L5_crpLANs (red) and L1-L5_rcpLANs (cyan) show no significant differences (ns; $\alpha = 0.01$). (**F**) Side view of pairs of volume-filled skeletons of Terminal LANs morphed onto a reference brain. crTerLANs (red) and rcTerLANs (blue) can statistically be discriminated, albeit marginally, by the number of AVs and PVs.

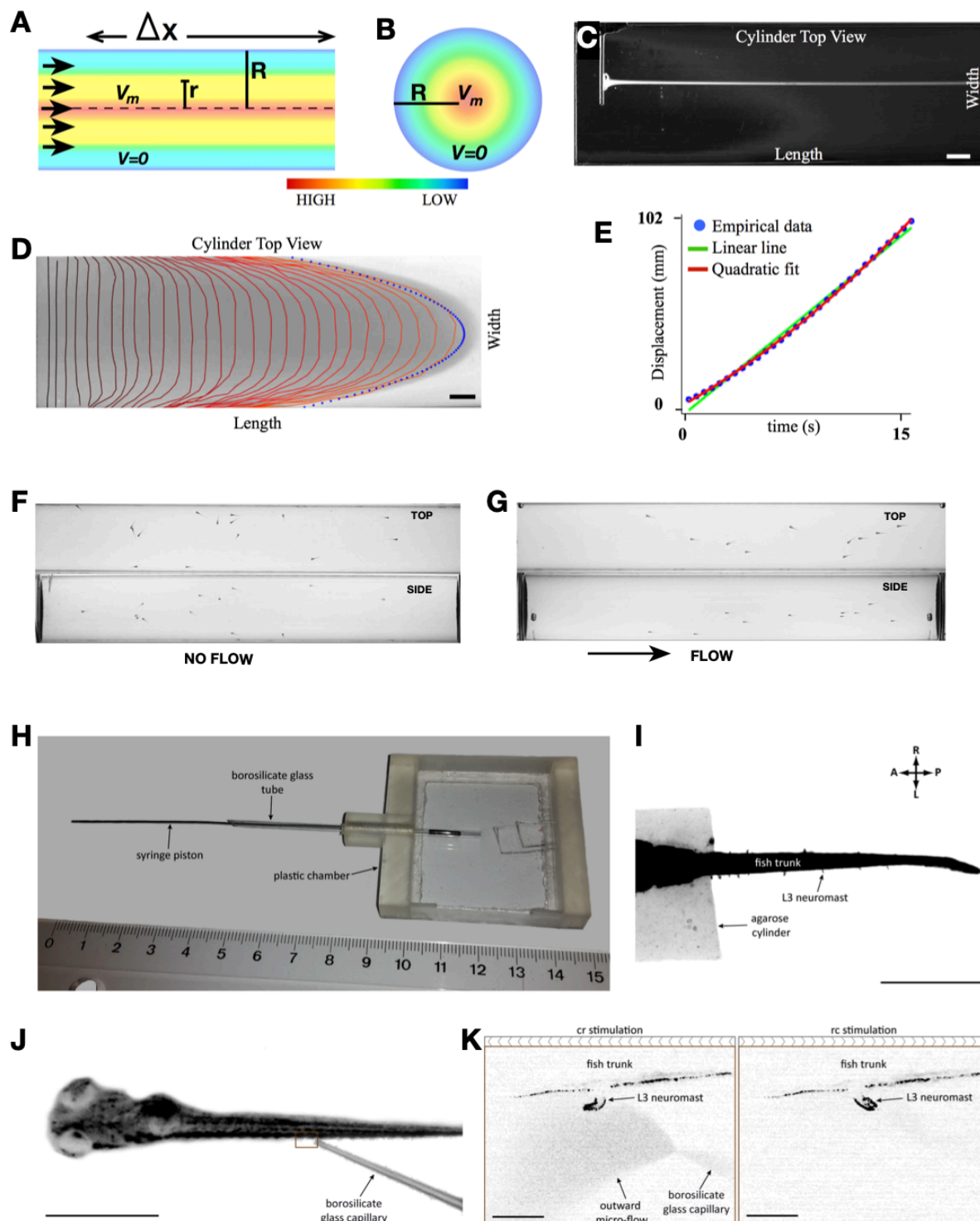


Figure S3. Experimental set-up for activity of lateralis neurons. Related to Figure 3 and 4. (A-B) Representation of a column of water moving at a constant velocity within a seamless cylinder, which generates an isosymmetric velocity gradient across the width of the cylinder. The rainbow-colored bar below the drawing describes the velocity gradient from high (red) to low (blue). Water flow is high in the center and low toward the periphery, being zero within the boundary layer between the water and the pipe's surface. (A) depicts a longitudinal and (B) a

transversal view of the cylinder. **(C)** Kymographs of the empirical test of water flow inside the rheotactic rig. A water-soluble dye (methylene blue) was delivered into the water through the tip of a syringe needle and videotaped. The straight line shows laminar flow at the center of the cylinder. **(D)** Kymographs of the empirical test of water flow inside the rheotactic rig. Here, the extreme of the cylinder closest to origin of the flow was filled with methylene blue and the displacement of the dye-front was videotaped and delineated in red at each time point. The flow velocity profile across the cylinder width is flat at the beginning of the movement and forms a parable when at full development, indicating laminar flow. **(E)** Plot of dye displacement (blue) at the center of the cylinder, fitting a linear increase (red). The slope of the fitted line is 6.8 mm/s while the plunger was moving at 5 mm/s. **(H)** Photograph of the mounting chamber. **(I)** An image of the trunk of a 7dpf larval zebrafish mounted in the chamber. The cupulæ of the neuromasts were labelled with fluorescent microspheres; red filter and green excitation light was used. **(J)** An image acquired by the camera of the two-photon setup showing the position of the electrode used for stimulation. Here and in (I), scale bars denote 1 mm. The area shown in (J) is outlined by an orange box. **(K)** Two-photon images of the L3 neuromast inclinations resulted from inward and outward microflow caused by stimulation, showing also the electrode tip filled with rhodamine solution and the outward flow during caudorostral stimulation. The stimulation electrode is not seen during rostrocaudal stimulation because negative pressure in the electrode results in filling it with non-fluorescent media from the chamber. The scale bars denote 100 microns.

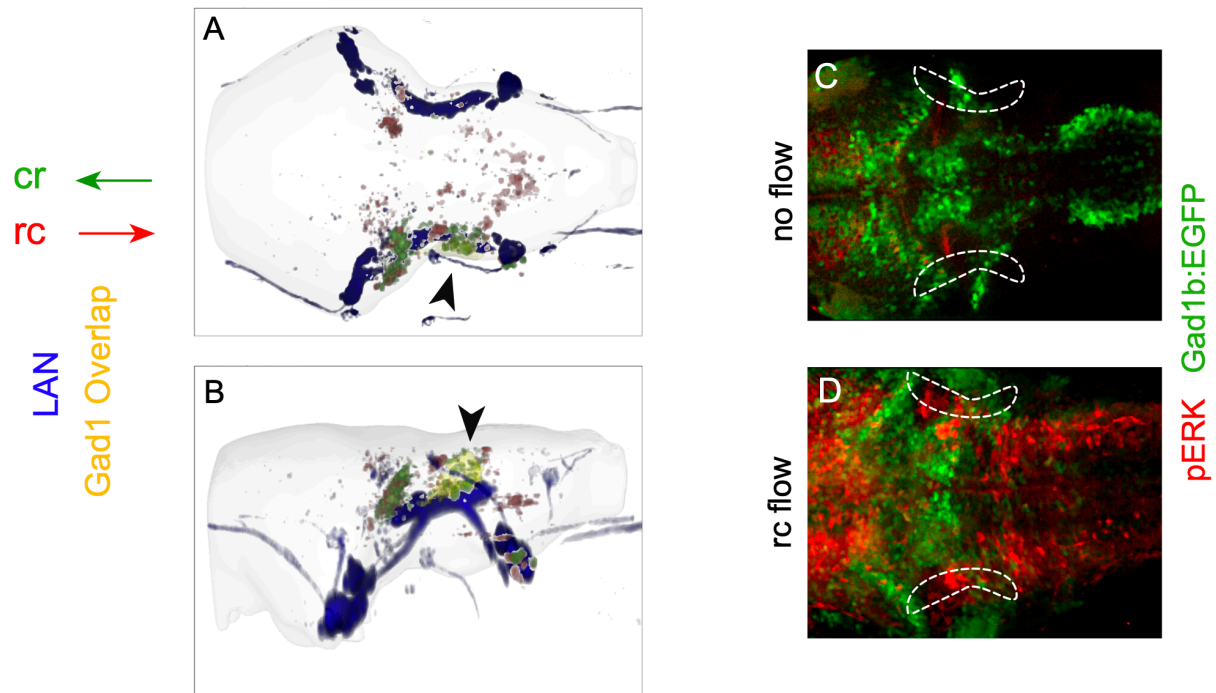


Figure S4. Mapping of neuronal activity in the hindbrain. Related to Figure 4.

(A-B) Dorsal (A) and lateral (B) views of a three-dimensional-reconstructed reference brain (transparent gray surface). Overlaid Sill:mCherry signal (blue), binary mask of the Gad1b signal (yellow), cr functional map (green), rc functional map (red). Note the overlap between the Gad1b signal and the cr functional map (indicated with a black arrowhead). (C-D) Dorsal view of a larval zebrafish expressing Gad1:EGFP (green) and immunostained with an antibody to pERK (red). (C) is a sample subject to no water flow, and (D) is a specimen maintained under continuous laminar water flow for 2 minutes. The white dotted areas indicate the location of the lateralis central lintel in the hindbrain (central arbors).

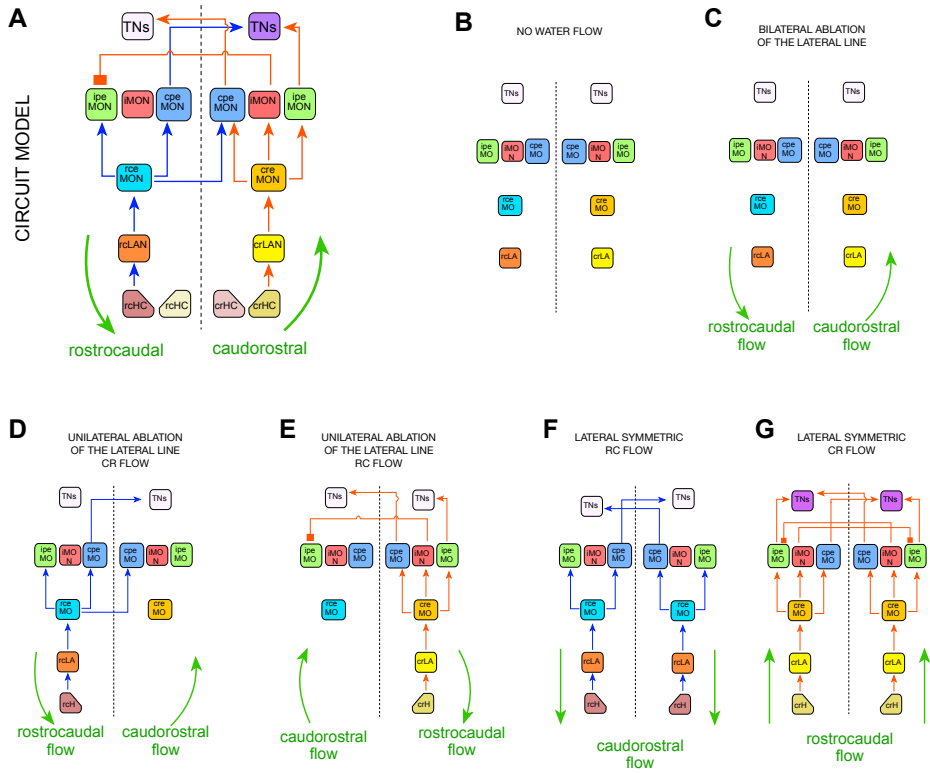


Figure S5. Assessment of the circuit model. Related to Figure 5. (A) Proposed circuit model. **(B)** The trivial situation in which under now flow, lack of stimulation of hair cells produces no sensory signal transmission and no activity in toral neurons (TNs) (lilac). **(C)** Identical outcome results from elimination of the lateral line in the presence of water flow. In this case, rheotaxis is disrupted. **(D-E)** Oteíza and colleagues have shown that when one side of the lateral line is eliminated, rheotaxis is severely impaired, indicating that $+/\emptyset$ does not provide enough information, and that the fish needs $+/-$ to determine flow direction. We have confirmed this result. The model circuit explains this result because if one side of the PLL is eliminated, directional information is persistently asymmetric, eliminating the capacity of the brain to use local rotational flow to determine flow direction. The model circuit captures the outcome regardless of the handedness of the local vortex: counter-clockwise in D and clockwise in E. **(F-G)** If the flow is lateral symmetric, no gradient across the horizontal plane develops, and the animals experiences no rotational flow around its body. In this case, the fish can detect the presence of flow, but it cannot determine its direction because it will experience no differences in flow regime after each swim bout. The model circuit also captures this feature because in cases of lateral symmetric rostrocaudal (F) or caudorsotral (G) flow, symmetry

cannot be broken and information transmission to the brain is vectorially ambiguous.